

Ekine Aristizabal Tolosa

**Finite element simulation for the cold-joining of
high power connectors**

Werkstofftechnik Aktuell

Schriftenreihe aus dem Fakultätsübergreifenden Institut
für Werkstofftechnik (IWT) an der TU Ilmenau

Herausgegeben von

Univ.-Prof. Dr. rer. nat. Dr. h. c. Peter Schaaf

und Univ.-Prof. Dr.-Ing. Edda Rädlein

Band 13

Die vorliegende Schriftenreihe "Werkstofftechnik Aktuell" berichtet über aktuelle Forschungsergebnisse aus dem Institut für Werkstofftechnik (IWT) der TU Ilmenau. Die ausgewählten Texte spiegeln die breit gefächerten materialwissenschaftlichen und werkstofftechnischen Themen, die am IWT bearbeitet werden, wieder. Für weitere Informationen und Rückfragen können Sie sich gerne an das Institut (www.tu-ilmenau.de/wt) wenden oder das Institut persönlich besuchen. Über Ihre Anregungen, konstruktive Kritik und Ihre Kontaktaufnahme würden wir uns sehr freuen. Das IWT steht wissenschaftlichen Zusammenarbeiten stets aufgeschlossen gegenüber.

Finite element simulation for the cold-joining of high power connectors

Ekine Aristizabal Tolosa



Universitätsverlag Ilmenau
2015

Impressum

Bibliografische Information der Deutschen Nationalbibliothek

Die Deutsche Nationalbibliothek verzeichnet diese Publikation in der Deutschen Nationalbibliografie; detaillierte bibliografische Angaben sind im Internet über <http://dnb.d-nb.de> abrufbar.

Diese Arbeit hat der Fakultät für Elektrotechnik und Informationstechnik der Technischen Universität Ilmenau als Dissertation vorgelegen.

Tag der Einreichung: 10. Februar 2015

1. Gutachter: Univ.-Prof. Dr. rer. nat. habil. Dr. h. c. Peter Schaaf
(Technische Universität Ilmenau)

2. Gutachter: Univ.-Prof. Dr.-Ing. habil. Jean Pierre Bergmann
(Technische Universität Ilmenau)

3. Gutachter: Dr.-Ing. Friedhelm Günter
(Robert Bosch GmbH)

Tag der Verteidigung: 11. Mai 2015

Technische Universität Ilmenau/Universitätsbibliothek

Universitätsverlag Ilmenau

Postfach 10 05 65

98684 Ilmenau

www.tu-ilmenau.de/universitaetsverlag

Herstellung und Auslieferung

Verlagshaus Monsenstein und Vannerdat OHG

Am Hawerkamp 31

48155 Münster

www.mv-verlag.de

ISSN 1868-6532 (Druckausgabe)

ISBN 978-3-86360-120-1 (Druckausgabe)

URN urn:nbn:de:gbv:ilm1-2015000249

Acknowledgments

This research work is the outcome of the cooperation between the Institute of Materials Engineering at the TU Ilmenau and Robert Bosch GmbH in Schwieberdingen. During these three years I had the great fortune to be supported by a number of persons my heartfelt thanks go to.

My thankfulness is first directed to my academic supervisor Univ.-Prof. Dr. rer. nat. habil. Peter Schaaf for his guidance and advice. Besides his expert opinion and supervision I gratefully acknowledge him the friendly welcome at his Institute and the pleasant cooperation. I would like to thank Univ.-Prof. Dr.-Ing. habil. Jean Pierre Bergmann for his interest on my work and being the second referee of this thesis. For the friendly atmosphere and their useful hints, I would like to thank my colleagues at the Institute of Materials Engineering.

My deepest gratitude is directed to Dr.-Ing. Friedhelm Günter for his engagement, supervision and his genuine interest on my personal wellbeing. My thank applies also to all my colleagues of the department Laser Material Processing, Electronic Packaging and Interconnection Technology at Robert Bosch GmbH. It has been a pleasure working with you.

I want to express my most affectionate gratitude to my parents for their love and unconditional support, which offered me this path of life.

Abstract

A method for the Finite-Element (FE) simulation of the Cold-Joining -Process (CJP) of massive copper contacts is developed in this thesis. The standard procedure for the calculation of interference fit connectors is not applicable to the joining process of massive copper components, since the contact area builds up in a context of considerable plastic deformation and high frictional loads. The new FE model not only shortens and optimizes the design cycle for novel High-Power-Connectors (HPCs), but also allows a deeper understanding of the CJP and the connector.

After a short introduction into the cold-joining technology and its relevance, the experimental details for the CJP and the general settings of the FE model are presented in the third chapter, as well as an overview of characteristic CJPs.

The main challenges of the FE simulation of CJPs arise in the fields of material and friction characterization. Therefore each of the two areas will be developed in a separate chapter, beginning with the state of the art in the field, and ending with the assessment of the impact of the new methodology developed.

The fourth chapter addresses the material characterization and includes two novel methods for the determination of flow curves and the characterization of the inhomogeneity at punched edges.

The friction behavior during cold-joining is studied in chapter five. A new test bench is developed for the determination of friction coefficients and the study of wear disposition.

Both material properties and friction behavior showed to be closely connected and interdependent. To cope with this complex interaction, both models were integrated in a FE tool. Guidelines are developed and proposed for an accurate FE representation of a certain CJP with the minimum modeling complexity.

The FE model is rolled out to real HPCs. The comparison between calculated and real features of the connector nails down the validity of the simulation. By means of this real example the capability of the new simulation method to set the ground for the design of future CJs is demonstrated.

Zusammenfassung

Im Rahmen dieser Arbeit wird eine neue Methode zur Beschreibung von massiven Kupfer-Einpresskontakte entwickelt. Die Berechnung von Pressverbänden nach DIN 7190 ist bei der Auslegung von massiven Kupferkontakten nicht anwendbar da während des Fügevorganges hohe Verformungsgrade und Reibspannungen auftreten. Das neue Modell bietet nicht nur verkürzte und effiziente Auslegungszyklen für neue Hochleistungskontakte (HLK) an, sondern vertieft auch das Grundverständnis des Fügeprozesses und der Kontakteigenschaften.

Nach einer kurzen Motivation des Themas und einer Einführung in die kalte Kontaktiertechnik, werden im dritten Kapitel die Grundlagen der experimentellen Arbeiten sowie der Simulationsmethoden erarbeitet.

Die Herausforderungen bei der Modellierung von Fügeprozessen liegen in der Materialbeschreibung und Reibungscharakterisierung. Deshalb werden die beiden Themen in zwei eigenständigen Kapiteln vorgestellt, ausgehend vom jeweiligen Stand der Technik bis zur Validation der entwickelten Methoden und Modelle.

Das vierte Kapitel beschäftigt sich mit der Materialbeschreibung und beinhaltet zwei neue Methoden zur bauteilnahen Ermittlung der Fließeigenschaften von Kupferwerkstoffen.

Das Reibverhalten in einem Einpressvorgang wird im fünften Kapitel untersucht. Hierzu wurde ein neuer Prüfstand zur Ermittlung von Reibkoeffizienten und Beschreibung der auftretenden Verschleißmechanismen aufgebaut.

Die Materialbeschreibung und die Reibungscharakterisierung sind eng miteinander verknüpft. Beide Modelle wurden deshalb in ein Finiten-Elementen (FE)-Tool zusammengeführt, um die komplexen Wechselwirkungen beschreiben zu können. Für eine genaue aber mit möglichst wenig Aufwand verbundene FE-Beschreibung von Einpressvorgängen werden Richtlinien erarbeitet und vorgeschlagen.

Auf Basis des FE-Modells werden neue Hochstromkontakte entwickelt. Über den Vergleich der simulierten und der realen Eigenschaften wurde das Modell erfolgreich validiert und seine Aussagekraft eindrücklich nachgewiesen.

Symbols

A_r	real contact area	mm^2
E	Young's modulus, elastic modulus	GPa
F	force	N
F_f	friction force	N
F_I	insertion force	N
F_I-x_I	force-displacement progression of an insertion process	
F_N	normal force	N
F_o	disassembly-load	N
F_T	tangential force	N
$F-x$	force-displacement progression	
G	shear modulus	GPa
HV	Vickers's hardness	DPH
k	shear limit of the softest material in a contact	MPa
K	stiffness matrix	N/m m
l_c	transversal length of contact zone	mm
m	shear model factor	
P	ploughing force	N
S	shear force	N
s	shear strength	MPa
s_1	shear strength of the softest material in a contact	MPa

s_2	shear strength of the joints in a contact area	MPa
v	velocity	m/s
v_L	longitudinal velocity	m/s
v_T	transversal velocity	m/s
x	contact penetration	mm
x_d	distance from the punched edge	μm
x_I	insertion distance	mm
α	Fraction of contact area that fails in the softest material	
μ	friction coefficient	
ρ	density	g/cm^3
σ_{CN}	critical normal stress in contact elements	MPa
σ_N	normal stress	MPa
σ_s	yield stress of the softest contact partner	MPa
σ_y	yield stress	MPa
τ	shear stress	MPa
ν	Poisson's ratio	

Acronyms

1D	One-Dimensional
2D	Two-Dimensional
CI	Confidence Index
CJP	Cold-Joining Process
CJT	Cold-Joining Technology
Cu-ETP	Electrolytic Tough Pitch Copper
E-	Electro-
EBSD	Electron Backscatter Diffraction
ECU	Electronic Control Unit
fcc	face centered cubic
FE	Finite Element
FEM	Finite Element Method
HLK	Hochleistungskontakt
HPC	High Power Connector
IDC	Insulation Displacement Connector
KANM	Kernel-based Analysis Method
PCB	Printed Circuit Board
SFE	Staking-Fault Energy

Contents

1	Introduction	1
1.1	Motivation.....	1
1.2	Main challenges and thesis goals.....	2
2	State of the art	5
2.1	Joining technologies for high power contacts.....	5
2.2	Introduction to the cold-joining technology.....	6
2.3	Limitations of existing knowledge	8
2.3.1	Analytical approach	8
2.3.2	Simulative approach	10
3	Cold-joining of high power connectors	11
3.1	Cold-joining process.....	12
3.1.1	Experimental details	12
3.1.2	Characteristic cold-joining processes	16
3.2	Finite element simulation of cold-joining processes	25
3.2.1	Solver	25
3.2.2	Contact properties.....	26
3.2.3	Mesh.....	28

4	Material characterization	31
4.1	State of the art.....	32
4.1.1	Introduction to the mechanical behavior of copper and copper alloys.....	32
4.1.2	Introduction to the determination of material properties 34	
4.1.3	Material models for the finite element method	34
4.2	Determination of material properties.....	35
4.2.1	Elastic properties.....	35
4.2.2	Plastic properties.....	36
4.2.3	Implementation of the material data.....	41
4.3	New method 1: Small-punch tests.....	48
4.3.1	Methodology.....	49
4.3.2	Validation.....	51
4.3.3	Results.....	52
4.3.4	Summary.....	55
4.4	New method 2: Local material characterization.....	56
4.4.1	Motivation and characterization of punched edges	56
4.4.2	Methodology.....	60
4.4.3	Validation.....	65
4.4.4	Results.....	66
4.4.5	Summary.....	73
4.5	Summary.....	73
5	Friction characterization	77
5.1	State of the art.....	78

5.1.1 Friction between metallic surfaces	78
5.1.2 Friction in the finite element method	80
5.2 Limitations of existing knowledge	82
5.3 Friction test bench	85
5.3.1 Experimental details	85
5.3.2 Validation.....	88
5.3.3 Results.....	90
5.4 Summary.....	99
5.4.1 Friction coefficient.....	99
5.4.2 Wear tendency	99
6 Implementation on the optimization of a real high power connector	101
6.1 Procedure for the optimization of a HPC	101
6.2 Optimization of a real HPC.....	104
6.2.1 Framework conditions.....	105
6.2.2 Results.....	105
6.3 New optimized connector	108
6.3.1 Samples	108
6.3.2 Cold-joining Process.....	112
7 Summary & Outlook	115
Publications	117
References	119
Appendix A	131

Chapter 1

Introduction

1.1 Motivation

Cold-joining is a remarkably profitable joining technology, owing to the simplicity of the assembly process, the low initial investment, and the possibility to join several contacts in parallel. In addition, heat dissipation and contamination with flux do not occur in this joining process.

Since the number of high power applications in the automotive industry is growing fast in the context of electro-mobility, increasing efforts are made in order to make this advantageous joining technology suitable for high power applications. Figure 1.1 exemplifies an application of cold-joining for a High-Power-Connector (HPC) in an electric car.

This technology is widely used for electronic components in telecommunications equipment, but its application in the automotive industry is mainly limited to elastic press-fit connectors in Printed-Circuit-Boards (PCBs) [No194]. Therefore, new design guidelines are needed for massive copper cold-joined connectors. Finite-Element-Method (FEM) models are still being developed for supporting the new design cycle.

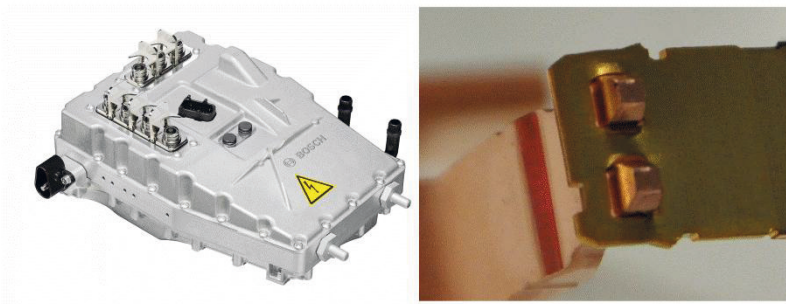


Figure 1.1: Left: direct current to alternating current inverter. Right: detailed view of the cold-joined HPC.

1.2 Main challenges and thesis goals

High currents demand massive contact components and large cross-sections. Therefore, the elasticity of the parts is not able to absorb geometrical tolerances and deviations in alignment of the components [Kan85]. In consequence, the main challenges to be faced to build up a simulation method for the Cold-Joining-Technology (CJT), derive from strong localized material loading.

These challenges take place in the fields of material and friction characterization, and will be separately studied in order to accomplish the following goals.

Regarding material characterization, one of the major challenges is the determination of the mechanical properties in the finished parts. This barrier has been overcome in *Chapter 4* pursuing these objectives:

- The determination of material properties for high plastic deformations.

- The consideration of the stress situation in the parts during the Cold-Joining-Process (CJP).
- The characterization of the material properties in finished parts and at punched edges.

The correct description of the frictional situation is the second foundation of a Finite-Element (FE) model for the CJT. High stresses in the contact zone lead to wear mechanisms that impede a robust CJP. An added value to the existing knowledge was generated in *Chapter 5*, being the solved questions:

- The determination of friction coefficients.
- The analysis of wear characteristics in close to real components.

Nevertheless, an isolated study of friction and wear mechanisms is not effective, since the contact area builds up by means of deformation of the assembly parts. Therefore, the interdependency between material properties, friction and the connector's geometry has to be represented.

The ultimate goal of this thesis is thus the implementation of accurate material and friction laws in a FE model that represents all these interdependencies.

Moreover, this work gives the guidelines for the design of new high power connectors. Instructions for the choice of the simplest friction and material characterization methods are given for an accurate FE modeling of a certain CJP.

Chapter 2

State of the art

This chapter introduces the cold-joining technology as an alternative for electrical contacting of massive copper components. The need of a simulative design tool is demonstrated.

The state of the scientific knowledge for the material and friction modeling will be separately presented in the corresponding chapters.

2.1 Joining technologies for high power contacts

The joining technologies are classified according to DIN 8593-0 into the following techniques [DIN03a]:

1. Assembling
2. Filling
3. Joining by mechanical means [DIN03b]
4. Joining by processing of amorphous materials
5. Joining by forming processes [DIN03c]
6. Joining by welding
7. Joining by soldering or brazing
8. Joining by means of adhesives

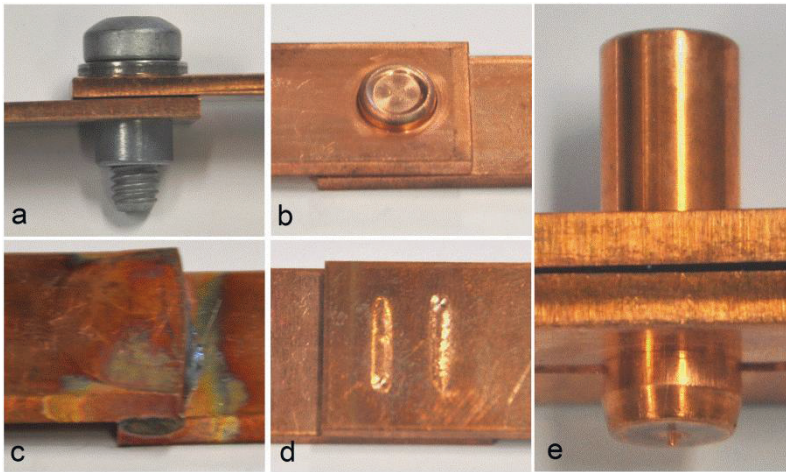


Figure 2.1: Overview of joining technologies for high power contacts: a) assembling, b) joining by metal forming, c) brazing/ soldering, d) (laser) welding, e) cold-joining.

The CJT is comprised in the third group, and offers a suitable alternative for the joining of HPCs. Potential joining technologies for high power applications are pictured in Figure 2.1 for the same joining function.

2.2 Introduction to the cold-joining technology

The CJT is an alternative to soldering and welding and comprises techniques that make and permanently maintain electrical contacts by purely mechanical means, without heat contribution. Connections joined by CJT are never opened after joining them once. This allows for high contact forces and significant plastic deformations during the CJP.

Cold-joining has been widely used since the 70s in the telecommunication industry in form of press-fit connectors. This technology has also found its application in the Electronic-Control-Units (ECUs) in the automotive industry [Nol94].

The family of CJC includes Insulation-Displacement-Connections (IDCs) and press-fit connections for PCBs and lead frames [Gün10]. Some exemplars of CJC are shown in Figure 2.2.

High power applications require fairly larger contact areas, and thus, greater insertion forces.

The massive cold-joining technology offers both electrical and mechanical joining of the components and is increasingly relevant in the context of the car electrification [Wit08].



Figure 2.2: Common cold-joined connectors in the automotive industry. Left: insulation displacement connectors. Center: Clamp connectors. Right: pin-through-hole connectors.

2.3 Limitations of existing knowledge

2.3.1 Analytical approach

Analytical approaches are used for the calculation of interference-fit joints [DIN01].

The norm DIN 7190 also accounts for plastic deformation of the components. Nevertheless, the reduction of the apparent contact area, due to plastic deformation during the insertion process is not considered.

The friction forces in the contact area of a CJC will determine not only the insertion forces, but also the retention forces during its working life, and thus its reliability [DIN03b, DIN01, Nol74, Sta11, Xie00].

A literature screening of friction coefficients between copper surfaces is shown in Table 2.1. Not only the broad spectrum of friction coefficients in dry condition require a targeted study of friction for HPCs, but also the knowledge gap about the onset of wear mechanism has to be acted upon.

Table 2.1: Literature overview of friction coefficients between copper surfaces.

Reference	Friction coefficient-Dry	Friction coefficient-Lubricated
[ASM92]	0.55	
[Bow53]	1	0.08
[Cho12]	0.1-0.14	
[Dav01]	0.55	
[Dav97]	1	0.08
[Dub94]	0.6-1	
[Pop11]	0.2	
[Smi04]	0.55	0.1

Figure 2.3 shows the insertion process of a real copper cold-joined connector. The analytical approach presented in DIN 7190 is adapted to the geometry shown in Figure 2.3 as follows [Dub94]:

$$F_I = \mu \cdot \sigma_s \cdot l_c \cdot x_I \quad (2.1)$$

The two friction coefficients for lubricated surfaces presented in Table 2.1 are applied in equation (2.1) for the prediction of the joining behavior pictured in Figure 2.3.

Figure 2.3 exemplifies the inapplicability of analytical approaches for the prediction of the insertion force peaks needed for the local plastic deformation of assembly parts (the interpretation of insertion force/ joining distance progressions is thoroughly discussed in *Chapter 3*).

Moreover, the analytical approach overestimates the insertion forces at the end of the joining process. Since this force is directly correlated to the retention force of the connector, the analytical approach would not deliver a conservative estimation of the connector's mechanical performance.

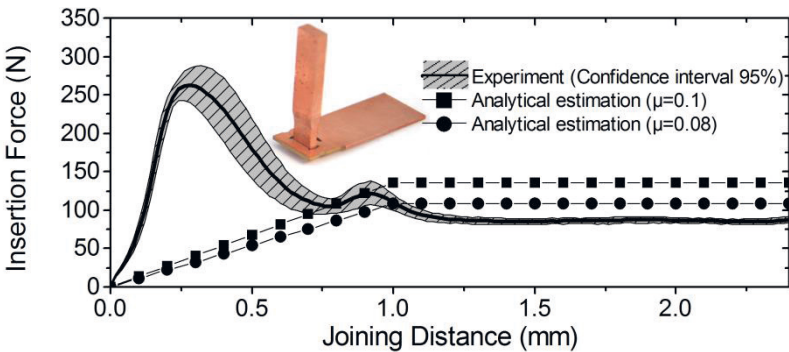


Figure 2.3: State of the art: Predictability of the cold-joining process of a real high power connector using an analytical approach.

2.3.2 Simulative approach

Simulation models have been developed mostly for the design and reliability studies of press-fit connectors [Mac03, Man07, Mer01, Kan85, Yam90].

Massive cold-joining connectors have been experimentally studied [Wit08], but the FE modeling of this kind of connectors has still not been approached.

Efforts for the in situ determination of material properties have been also applied to the press-fit technology [Man07]. Yet a non homogeneous material behavior was never modeled, and the issue of the anisotropic behavior has not been addressed for the force-fitting simulation.

The modeling of the friction between pin and printed circuit board has been a recurrent topic. Most models are based on Coulomb's friction law [Mer01, Kan85, Yam90], and custom made friction laws have also been evaluated [Cor03, Man07, Toh06]. The affinity of copper components to different wear mechanisms has on the other hand never been assessed for CJP's.

More details to the scientific knowledge for the material and frictional modeling will be clarified in the corresponding chapters.

Chapter 3

Cold-joining of high power connectors

The design of a CJC comprehends its geometry, the material combination, and the frictional state between both components. All three aspects are interdependent, therefore not only a general view of the CJP is necessary, but also validated models for the material characterization and frictional behavior.

Therefore the material and frictional models will be developed and validated in distinct chapters. This chapter deals with the CJP and its general FE modeling. On the one hand, it compiles the experimental details of the CJPes based on which the simulation models will be validated. On the other hand, the optimized set ups of the general FE model will be presented.

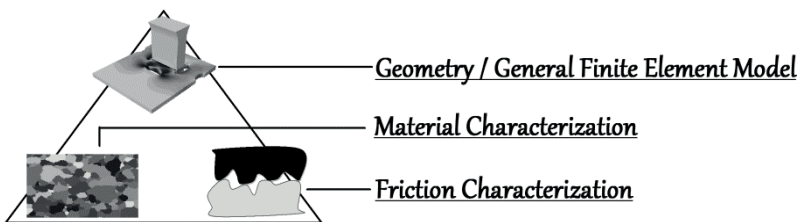


Figure 3.1: Overview determining factors in a cold-joining process.

The validation of FE simulations for CJPes is carried out via comparison between experimental and simulated force-displacement (F_I-x_I) progressions of the insertion process. These F_I-x_I curves represent valuable information of the CJPes. Therefore, characteristic CJPes will be interpreted in this chapter based on their F_I-x_I progressions.

3.1 Cold-joining process

Massive cold-joined connectors are permanently joined by purely mechanical means and never opened again.

The difference between the dimension of the male component and the female component in the contact area, that is to say the overlapping length between both components, is defined as overlay. The overlay is elastically and plastically deformed to build the connector, and determines the joining forces, the frictional situation, and the connector's reliability.

3.1.1 Experimental details

Samples

Massive copper CJs are joined in two different geometrical configurations.

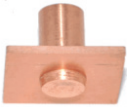
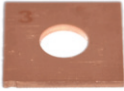




Electrolytic-Through-Pitch-Copper (Cu-ETP) is the commonly used contact material. In this work bronze alloys are also included due to their higher mechanical strength and lower cost. More detail about the material selection will be given in *Chapter 4*.

Table 3.1 presents the samples used for the study of CJPes. The *configuration A* layout was chosen for its axial symmetry. Cylindrical copper bolts are turned and grinded to size and inserted in the stamped female components. The experiments

carried out in this configuration serve the purpose of optimizing the general settings of the FE model with a low numerical expense. Moreover, different wear mechanisms are investigated on the basis of this configuration.

The *configuration B* design was chosen as a close instance of CJPes in series production. Both the male and female components are stamped from a 2 mm copper sheet.

Table 3.1: Samples for experimental study of CJPes. The different geometrical designs are denominated as *configuration A* and *configuration B*. The numbers represent the overlay between components and its 95% confidence interval in μm . Each material combination is studied in three different overlays.

Configuration A		Female Component			
					
Male Component		Cu-ETP R200	Cu-ETP R250	Cu-ETP R290	CuSn ₀₁₅ R290
		36 ± 1	32 ± 1	31 ± 1	31 ± 1
Cu-ETP R250		56 ± 1	52 ± 1	51 ± 1	51 ± 1
		75 ± 1	71 ± 1	70 ± 1	70 ± 1
Configuration B		Male Component			
					
		Cu-ETP R200	Cu-ETP R250	CuSn ₆ R500	
Female component		33 ± 6	36 ± 7	32 ± 6	
	Cu-ETP R200	50 ± 6	51 ± 6	50 ± 5	
	Cu-ETP R250	39 ± 5	41 ± 6	38 ± 5	
	CuSn ₆ R500	55 ± 5	57 ± 5	55 ± 4	
		47 ± 6	50 ± 7	46 ± 6	
		63 ± 5	65 ± 5	63 ± 5	

The components are cost-efficiently produced in a single die-cutting step. The geometrical tolerances are good enough to assure a reproducible joining process.

A new inhomogeneous material law for punched edges is developed by means of the *configuration B* components. This configuration is also optimized to avoid wear and therefore used to measure friction coefficients between copper surfaces and study the propensity of copper materials to adhesive wear.

Every geometry and material combination layout is tested in a broad range of overlays to prove the validity of the simulation model for geometry optimizations.

An accurate measurement of the overlays is essential for the modeling of the CJP. Other relevant dimensions for the building of the contact area, such as sheet thicknesses and contours were also measured.

The dimensions of the inside diameters of both female geometries were optically measured with a Mycra SL 440. The male components in *configuration A* were also measured with a Zeiss Prismo Navigator optical system. This enabled the highly precise overlay measurements presented in Table 3.1.

A punched edge is formed, as represented in Figure 3.2, by a die roll, a straight cut, and a fracture area. A Mahr LD 120 was used to measure the geometry of the punched edges, the roughness of the surfaces, and the radii of the male components in *configuration A*.

These measurements allowed the exact representation of the die roll and the straight cut in the simulation model.

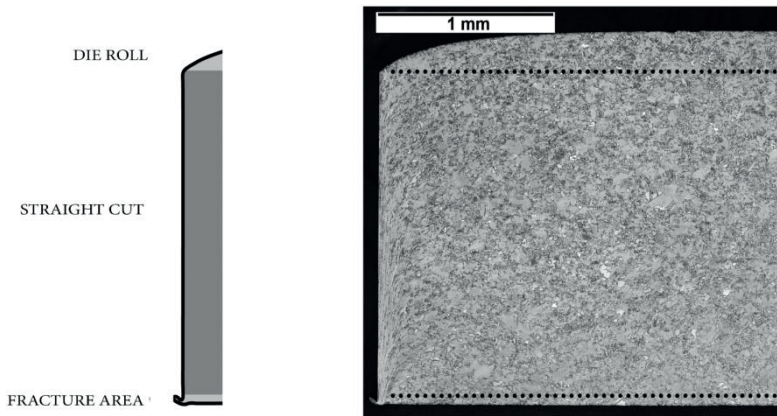


Figure 3.2: Structure of a punched edge, formed by the die-roll, the straight cut, and the fracture area.

The fracture area was not considered in the modeling due to the small area that represents, as shown in the cross-section of Figure 3.2.

Cold-joining

All CJPes are carried out in a Zwick Z010 static material testing machine and F_I - x_I data are collected.

The joining speed was set to 20 mm/min, which is a realistic value for series production. Nevertheless, no rate dependent phenomena takes place during the joining process and all simulation models are considered static.

The joining instruments designed for the CJPs in *configuration A* and *configuration B* are represented in Figure 3.3.

The compliance of the machine for each setting is discounted from the measured F_I - x_I progressions.

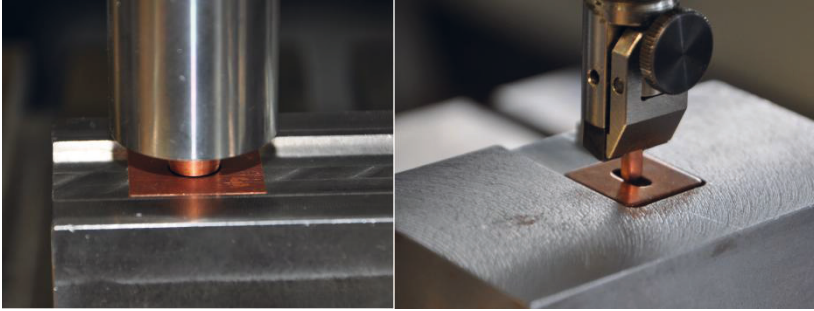


Figure 3.3: Experimental setups for cold-joining processes. Left: setup for *configuration A*. Right: setup for *configuration B*.

For the purpose of the model's validation for different friction situations, the CJP is carried out in two different lubrication conditions: in delivery condition (which may contain an undefined amount of machining lubricants) and relubricated (see *Appendix A*).

3.1.2 Characteristic cold-joining processes

In this section, characteristic F_1 - x_1 progressions during CJPs are presented and interpreted, and are used as basis for many considerations in following chapters.

The plastic deformation of one or other contact partner, and thus, the consequent formation of contact area depends on the relative strength of the materials of both components.

On the other hand, the propensity of copper materials to wear depends on the hardness difference between the surfaces.


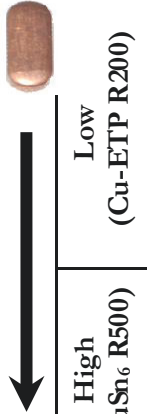
Therefore, different frictional states and characteristic F_1 - x_1 progressions can be classified according to the relative strength between the materials of both assembly parts. That is why materials were selected in order to cover a broad spectrum of

mechanical strengths, being the softest material Cu-ETP R200 and CuSn₆ R500 the hardest one.

An overview of the classification of CJPes, according to the strength difference between components, is presented in Table 3.2.

These characteristic joining processes are represented from Figure 3.4 to Figure 3.8, on the basis of different contact layouts joined in *configuration B*.

Table 3.2: Overview of characteristic cold-joining processes depending on the relative strength of both contact partners.

		Strength of female component	
			
		Low (Cu-ETP R200)	High (CuSn ₆ R500)
Strength of male component	 Low (Cu-ETP R200)	CASE 1A: Plastic deformation of both assembly parts CASE 1B: Adhesive wear	CASE 2: Chip formation
	High (CuSn ₆ R500)	CASE 3: Major plastic deformation of female component	CASE 4: Plastic deformation of both assembly parts

Different contact and frictional situations can be detected solely by the examination of a F_I - x_I curve. The F_I - x_I progressions from Figure 3.4 to Figure 3.8 are normalized (both forces and joining distances) for a better comparison between the presented cases.

The friction interaction between both components for each of the cases represented in Table 3.2 will be further discussed in Chapter 5.

Figure 3.4 represents *case 1A*. The cross-section was made at an

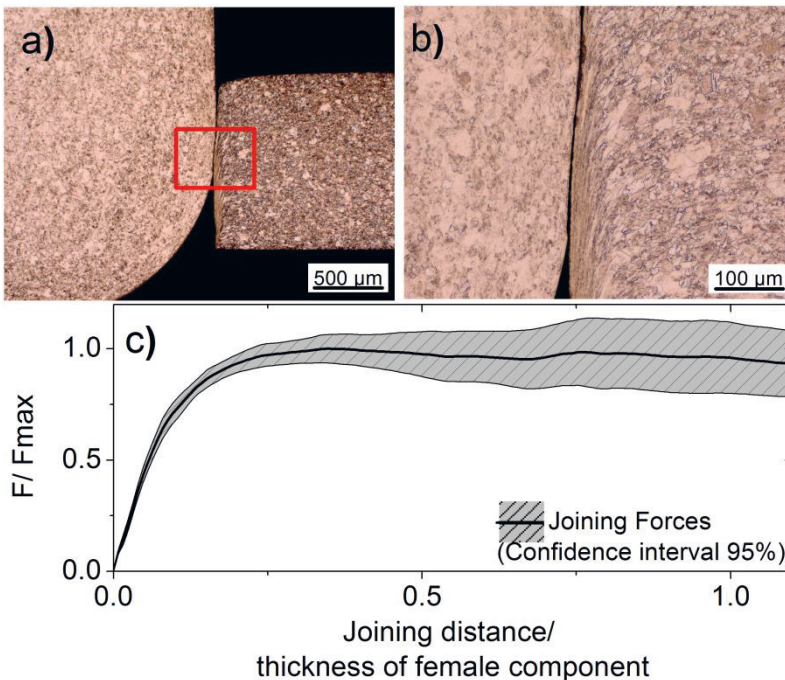


Figure 3.4: *Case 1A*. a) Characteristic contact zone in a CJC composed by two soft copper components. b) Detailed view of the plastic deformation of both assembly parts during the CJP. c) Characteristic F_I - x_I progression for a *case 1A* CJP.

insertion distance of 1 mm (halfway through the female component) and shows the plastic deformation of both components during the CJP. The insertion force does not appreciably increase during the joining process after the plastification of both components.

Case 1B is displayed in Figure 3.5. A positive substance joining is observed in the cross-section. This kind of strong substance-to-substance joining is known in the CJT as “cold-welding”. The onset of cold-welding produces the high scattering of joining

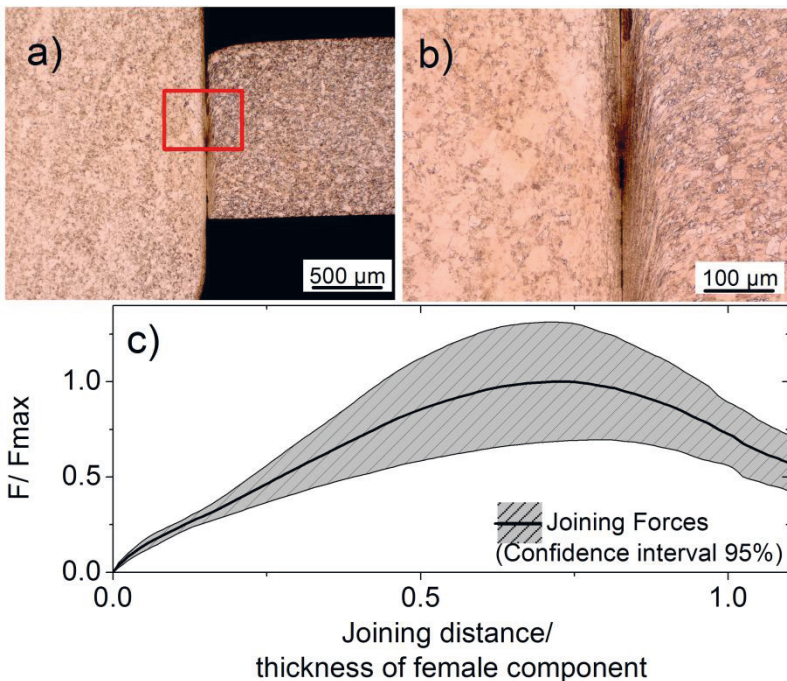


Figure 3.5: *Case 1B.* a) Characteristic contact zone in a CJC composed by two soft copper components that cold-welded. b) Detailed view of the adhesion between both components. c) Characteristic F_1-x_1 progression for a CJP with severe adhesive wear between components.

forces observed in Figure 3.5-c. The decrease of joining forces before reaching the whole thickness of the female component is due to the rupture of these joints.

Due to the high fluctuations in the series process and the unpredictable rupture of joints, this case has to be avoided. *Case 1B* is easily detectable on the basis of a F_I-x_I curve. Not only the bell-shaped curve, but also the unexpectedly high joining forces with regard to *case 1A* (see Table 3.1) are an indication of cold-welding.

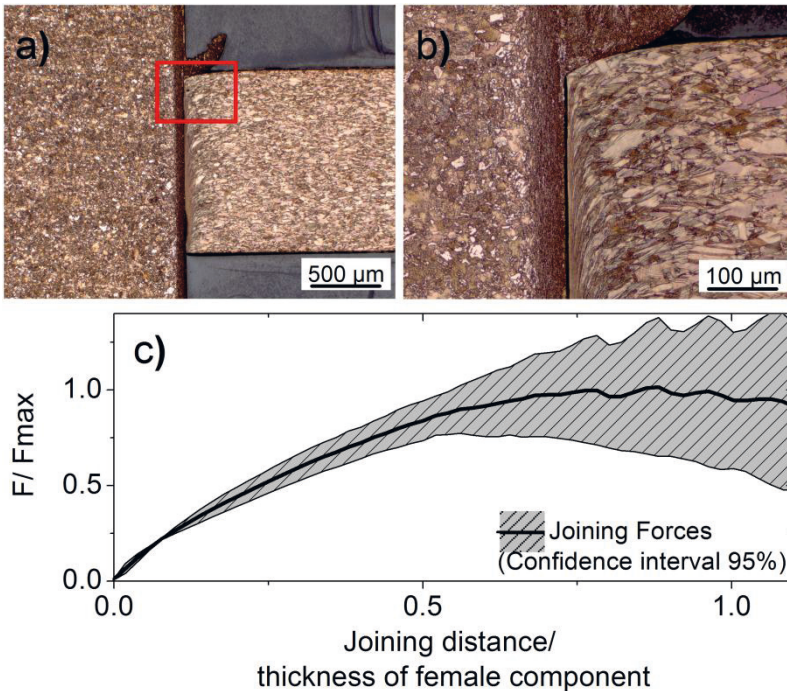


Figure 3.6: *Case 2.* a) Characteristic contact zone in a CJC composed by a soft male component and a hard female component. b) Detailed view of the dip formation during the CJP. c) Characteristic F_I-x_I progression for a *case 2* CJP.

Cold-welding corresponds to an adhesive wear behavior, and takes mostly place when two soft copper components are joined. The disposition of different materials to adhesive wear and the main influence factors will be further discussed in *Chapter 5*.

If a soft material is pressed into a much harder female component, the outer assembly part will rub the soft material off. The chip formation can be identified in the cross-section of Figure 3.6. Just as the cold-welding exemplified in *case 1B*, *case 2* has to be prevented, since it also leads to an unstable CJP.

The onset of chip formation is frequently visible to the naked eye in the CJC. *Case 2* is also clearly recognizable in its F_1-x_1 progression by the observation of non robust CJPEs with disproportionately high joining forces (see absolute maximal joining forces in Table 3.3).

The opposite material combination to the one studied in *case 2*, is considered in Figure 3.7. The insertion of a hard material into a soft one delivers a robust process. The cross-section reveals a major plastic deformation of the softest material.

The force progression in Figure 3.7 is a very characteristic curve of many cold-joined and press-fit connectors, and has already been interpreted for massive CJCs by Erdogan [Erd07].

The constant force reached at the end of the joining force corresponds to the friction load between both surfaces. Higher insertion forces occur during the CJP, even though the contact area is still not fully formed. These high forces directly correlate to the energy needed to plastically deform and move the large volume of material pile up visible in the cross-section of Figure 3.7.

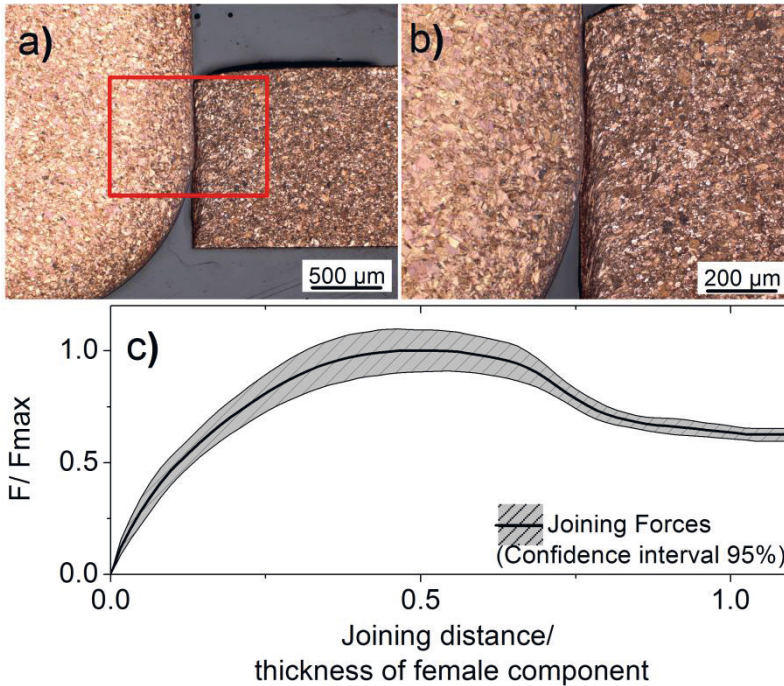


Figure 3.7: *Case 3.* a) Characteristic contact zone in a CJC composed by a hard male component and a soft female component. b) Detailed view of the plastic deformation of the female component during the CJP. c) Characteristic F_{1-x_1} progression for a *case 3* CJP.

A high insertion force peak may lead to a too high plastic deformation and thus to a lower contact area and friction force. The overlay has to be adjusted for an optimized utilization of the material's strength.

From the frictional point of view, *case 3* is an advantageous material combination: abrasive chip formation (*case 2*) can be avoided by a correct geometrical design, and the susceptibility to adhesive wear (*case 1B*) is low due to the high hardness difference between components.

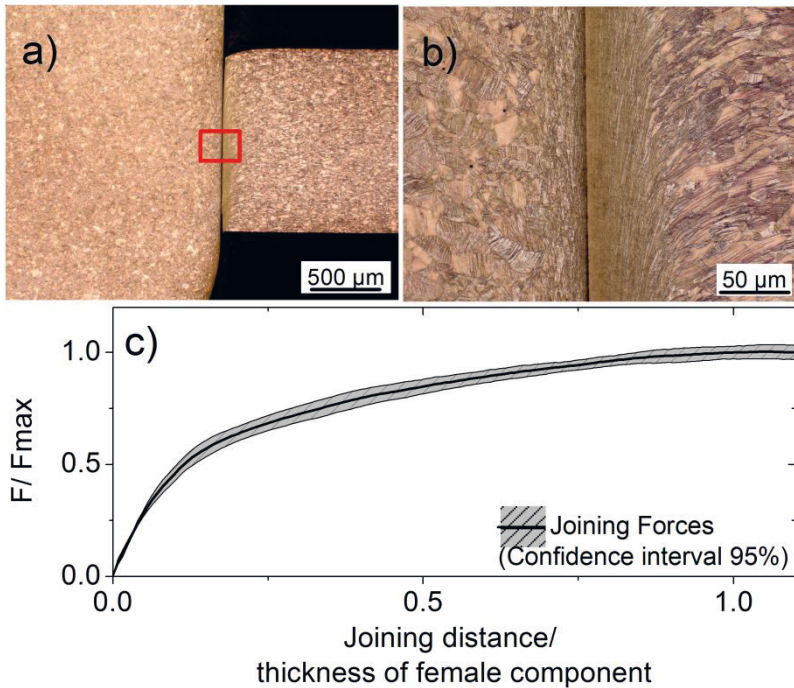


Figure 3.8: *Case 4.* a) Characteristic contact zone in a CJC composed by two hard CuSn_6 components. b) Detailed view of the contact area. c) Characteristic F_1-x_1 progression for a *case 4* CJP.

Figure 3.8 corresponds to *case 4*. The high strength of the bronze alloy compared to the Cu-ETP leads to a very robust joining process.

Since the perfectly plastic behavior of the material is not reached, *case 4* offers permanently ascending joining forces. Higher overlays are conceivable in this case, since higher retention forces would be accomplished. The disposition to adhesive wear is accordingly lower compared to the *case 1* CJPes, due to the higher strength of the material.

Table 3.3: Maximal insertion forces and their 95% confidence interval of the CJPs represented from Figure 3.4 to Figure 3.8.

	<i>CASE 1A</i>	<i>CASE 1B</i>	<i>CASE 2</i>	<i>CASE 3</i>	<i>CASE 4</i>
$F_{I,\max}$ (N)	66 ± 6	277 ± 89	748 ± 320	145 ± 15	165 ± 10

Not only the shape of a F_I - x_I curve, but also the absolute values of the joining forces are characteristic for the different cases presented in this section. Table 3.3 concentrates the maximal insertion forces observed in each CJP displayed from Figure 3.4 to Figure 3.8.

For an equivalent material combination and overlay, *case 1A* and *1B* show clearly different insertion forces. Therefore, adhesive wear can be also detected by the observation of unexpectedly high insertion forces (up to five times higher than the expected forces without adhesive wear).

The disproportionate insertion forces observed in *case 2* are also characteristic of chip formation, in addition to the unpredictability of the process.

For *case 3* the maximal insertion force in Table 3.3 does not correspond to the retention force. Both relevant values are determined by the strength of the weakest material.

The highest joining force in a robust process is reached in *case 4*.

This classification of CJPEs serves the purpose of interpreting F_I - x_I curves, and sets the basics for the preferred material combinations: those which deliver high retention forces with no risk of wear mechanisms.

This insights will be transferred to a methodology of CJC's design in *Chapter 6*.

3.2 Finite element simulation of cold-joining processes

This section describes the basic settings of the Finite Element Models presented in this work.

The FEM is a numerical procedure for the solution of differential equations. Variational methods are used to minimize error and reach a stable solution: the Newton-Raphson method is used in this work.

The application of the FEM to complex continuous structures is based on their idealization in a discrete number of “finite elements”. All sets of element equations are systematically recombined into a global system of equations.

The main challenge of applying the FEM to the massive CJT is the strong non-linear nature of the problem. All three causes for a non-linear behavior of the simulation are present in a CJP: 1) The non-linearity caused by the material, due to the strong plastic deformation, 2) The strong non-linear behavior caused by the contact between assembly parts, 3) The geometrical non-linearity as a result of the large displacements and strains in the elements close to the contact area [Nas10, Stel08].

3.2.1 Solver

No time-dependent material or frictional behavior is observed, as long as the joining speed is kept in the practicable range applied in the series production. Therefore, a static analysis is suitable for the simulation of the CJP.

Nevertheless, explicit time integration was assessed for the solving of the CJPes. The highly non linear nature of the problem

may make explicit time integration numerically favorable in comparison to a static implicit solution.

Explicit time integration showed no significant improvement on the computing time.

Moreover, the implicit solver offers a converged solution with the necessary mesh density for an accurate solution of all CJPes, except the joining processes classified as *case 1B* and *case 2*. These joining behaviors are to be avoided and therefore no FEM model is necessary.

Basically, the implicit solver can solve with the same numerical expense and a better accuracy all relevant CJPes.

Thus, all simulation results shown in this work are generated by an implicit solver. Explicit solvers may become relevant and convenient for a shorter computing time, if large three dimensional models have to be solved or the parallelization capability of these algorithms improves.

The commercial FEM tool ABAQUS was used in this work.

3.2.2 Contact properties

A correct contact formulation between assembly components determines the accuracy and convergence behavior of the simulation for a CJP.

The balance of the forces in the system depends on the contact area, where all forces between boundary conditions and loads are transmitted.

The contact in normal direction was defined as “penalty-contact”. This algorithm creates a force in normal direction between both assembly parts, which is proportional to the penetration between surfaces.

This solution was compared to the results delivered by a normal contact formulation with lagrangian multipliers. This method includes new degrees of freedom in the system, and thus, the penetration between contact surfaces is zero. This contact definition is therefore closer to reality, but requires a higher computational cost.

Since the penalty method and the completely rigid contact formulation delivered the same results and accuracy, all the results shown in following chapters correspond to a penalty contact formulation, due to its better convergence behavior.

The contact in tangential direction describes the frictional behavior during the joining process and will be thoroughly discussed in *Chapter 5*.

The contact discretization is addressed in the following section, which deals with the meshing.

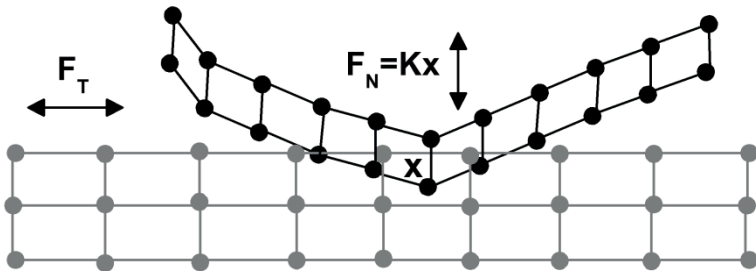


Figure 3.9: Schematic representation of the mesh of both contact partners and the contact formulation between them.

3.2.3 Mesh

The mesh in the contact area is indispensable for the convergence of the simulation and the convergence and accuracy of the solution, since the all loads present in the system are transmitted in this area.

High material loading and deformation occur in the contact area. These high local stress gradients require extremely fine meshes to be accurately represented in the simulation model. That is why, a regular mesh structure with a high density is necessary in the contact area.

The necessary mesh density in this zone for an accurate solution depends on the material combination and the structural stiffness of the assembly parts.

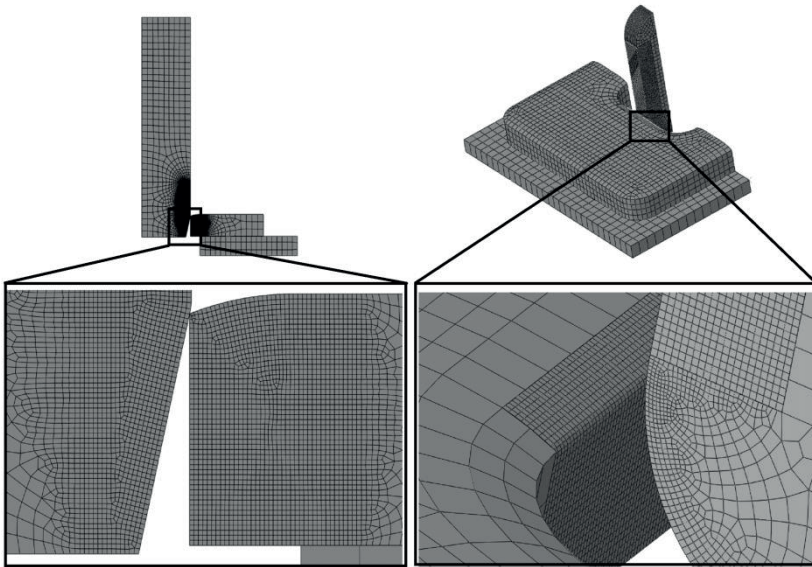


Figure 3.10: Left: mesh for the simulation of *configuration A* geometries and detailed view of the contact area. Right: mesh for the simulation of *configuration B* geometries and detailed view of the contact area.

That is why the meshing has been optimized distinctly for the different contact geometries and material combinations as shown in Figure 3.10.

The mesh size was adjusted to the minimal mesh density which delivered a constant first order solution (an accurate F_1-x_1 progression is pursued).

As reference values to start a mesh density analysis, a mesh fineness of $30\ \mu\text{m}$ is proposed for rigid peripheries around the contact area (similar to *configuration A*), and a mesh size of $60\ \mu\text{m}$ for assembly parts that are able to elastically absorb the deformation during joining (similar to *configuration B*).

Regarding the element types, linear axially symmetric elements are used for the simulations in *configuration A* and linear three dimensional volume elements in *configuration B*.

Chapter 4

Material characterization

The outstanding electrical and thermal conductivity of copper, as well as its strength, and fatigue and corrosion resistance, are the properties that make this material the preferred choice for HPCs. Bronze alloys are applied if a higher strength is required [Dav01]. This chapter deals with the material description of copper and copper alloys for the CJT.

The material behavior of the components determines the contact area that builds up during cold-joining. The correct characterization of the relative strength between both contact partners has a special relevance, since the plastic deformation of one or other assembly part dictates the structure of the contact area and the course of the joining process (section 3.1.2).

The main challenges in order to build a material law for the massive cold-joining simulation derive from the ductile nature of copper, which goes through considerable changes in material behavior during the production process of the components. This may lead to anisotropic or inhomogeneous material behavior of the parts, and thus to a more complex material model.

Therefore, the characterization of finished parts and new methods for the in situ determination of material properties are discussed in this chapter.

4.1 State of the art

4.1.1 Introduction to the mechanical behavior of copper and copper alloys

Copper has a face-centered-cubic (fcc) crystalline structure. Both the ductility of this metal and its electrical and thermal conductivity can be explained by its relatively weak metallic bonds.

Copper as contact material

In addition to its good thermal and electric conductivity, copper offers as contact material a very good machinability.

The main drawback of copper as contact material is its tendency to form oxide layers and its sensitivity to Sulphur compounds. This may lead to a high contact resistance and requires a strong friction during switching for the removal of these layers. Nevertheless this inconvenience does not apply to the massive CJT, since the contacts are permanently joined and gastight. Moreover, the high joining forces ensure the elimination of oxide films during joining [Dav01, Ign00, Wie98].

Plastic behavior of copper

Slip in a single fcc crystal occurs along its $\{111\}$ close packed planes. The Cu-ETP and bronze materials studied in this chapter are however polycrystalline.

The diverse die rolled Cu-ETP sheets may differ in their yield strength from 100 MPa to >320 MPa. The different mechanical properties in this polycrystalline material are achieved by hardening mechanisms. Mainly grain boundary strengthening and work hardening contribute to the increased strength of the examined copper materials [Rös12].

Low alloy copper materials display a considerably improved material strength and a low detriment of the electric conductivity [Dav01, Wie98]. Therefore, bronze alloys are included in the test plan of the following chapters.

Copper shows a temperature dependent flow behavior [Wie98, Mit04]. The strength of the material strongly decreases at elevated temperature. Due to the slow joining velocities at room temperature, and the outstanding heat dissipation from the contact area into the copper components, no temperature dependency of the material is considered in the CJT.

The rate dependent flow behavior of copper is also more pronounced at elevated temperatures. Polycrystalline fcc metals display a low rate dependency [Mit04, Nag67]. Therefore, no rate dependent behavior of copper will be considered in this chapter.

Texture of copper

The die-rolled copper sheets and the cold-drawn copper bars will reflect the direction of deformation [Dav01]. The grains of the metals, the grain boundaries and second phases tend to become elongated in the direction of cold work.

This affects the mechanical behavior of the metal, making an anisotropic material law necessary in some cases.

On the other hand, tensile-compression asymmetry has been observed in polycrystalline copper and to some extent attributed to texture [Böh03, Len55, Yap07].

Anisotropic behavior and texture will be therefore examined in this chapter.

4.1.2 Introduction to the determination of material properties

Tensile tests are the most broadly used method to characterize the elastic-plastic behavior of metals [Fuh03, Die94].

However, flow curves for high strains are needed for the description of processes, where high localized plastic equivalent strains take place. Tensile curves would need to be in these cases extrapolated for strains after the necking. Torsion experiments, hydraulic deep drawing tests, compression layer tests, and ring compression tests, are amongst others, applied for the determination of these flow curves [Eck09, Ges03].

This chapter presents flow curves based on optically assessed tensile tests (real strains calculated also after the necking) and compression tests.

Moreover, specific methods for the determination of material properties for the CJT will be presented in the following sections.

4.1.3 Material models for the finite element method

Isotropic elasticity and plasticity with isotropic hardening are the standard implemented material models for the FE simulation of force-fitting processes [Kan85, Man07, Mer01].

Anisotropic behavior of metal sheets is however contemplated in metal forming simulations [Eck09, Kob89], and will also be assessed in this work.

Isotropic hardening will be assumed in all material descriptions, since just the CJP will be simulated. Hardening descriptions would need to be assessed for simulations with cyclic loading, such as reliability studies on the CJs.

4.2 Determination of material properties

4.2.1 Elastic properties

The measurements of elastic properties for the material model have been carried out by means of an ultrasonic test system (Krautkramer USLT 2000), according to the norm DIN EN 843-2.

The determination of the material's density is necessary for the calculation of the elastic properties from the sound's velocity in the material. The determination of the samples' density was accomplished according to the Archimedes' principle, as stated in DIN EN 623-2.

Equations (4.1) to (4.3) were applied for the calculation of the elastic properties.

$$v = \frac{2 \text{ Thickness}}{\text{Roundtrip transit time}} \quad (4.1)$$

$$\nu = \frac{1-2(v_T/v_L)^2}{2-2(v_T/v_L)^2} \quad (4.2)$$

$$E = \frac{\rho (1+\nu)(1-2\nu)v_L^2}{1-\nu} \quad (4.3)$$

The results are represented in Table 4.1.

No elastic anisotropy could be measured in the rolling direction and its perpendicular one in the copper sheets. Nevertheless, a decrease of Young's modulus is measured for the more work-hardened materials. The phenomenon has already been documented [Wie95] and is attributed to the material's texture [Böh03].

Table 4.1: Ultrasound characterization of elastic properties in copper materials.

	ρ [g/cm^3]	E [GPa]	G [GPa]	ν
Cu-E'IP R200	8.91	130	48.0	0.35
Cu-E'IP R250	8.91	125	46.5	0.35
Cu-E'IP R290	8.91	118	43.2	0.36
CuSn₀₁₅ R290	8.91	126	46.6	0.35
CuSn₆ R500	8.86	120	44.0	0.36

4.2.2 Plastic properties

Tensile tests in sheet material

Different copper sheets used to manufacture the components for *configuration A* and *configuration B* connectors were characterized by means of optically assessed tensile tests. Three samples were assessed for each material in the rolling direction and another three in its perpendicular direction.

The probes were produced according to the DIN 50125 norm and stochastically indexed, to allow the optical real strain calculation.

The tensile tests were performed according to the norm DIN EN ISO 6892.

Figure 4.1 shows an example of a material characterization for Cu-E'IP R200 samples. One of the samples was evaluated with a strain gauge, which illustrates the wider spectrum of strains that the optical systems can evaluate. Otherwise, the tensile tests are highly reproducible.

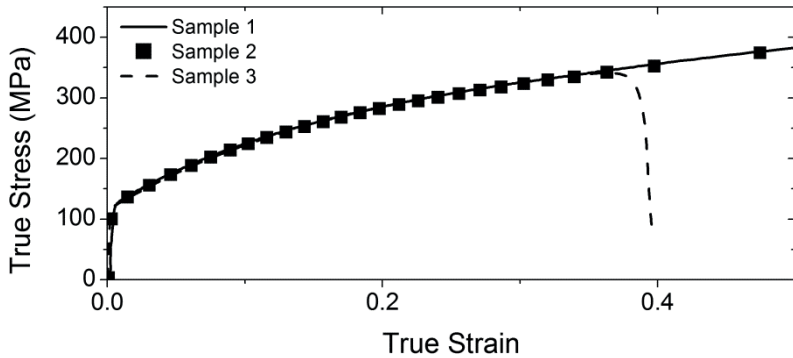


Figure 4.1: Example of tensile tests for the material Cu-ETPR200 in rolling direction. The strains have been optically assessed for samples 1 and 2, and a tactile strain gauge has been used for sample 3.

The average flow curve in rolling direction for each material is shown in Figure 4.2. The error bars are not noticeable.

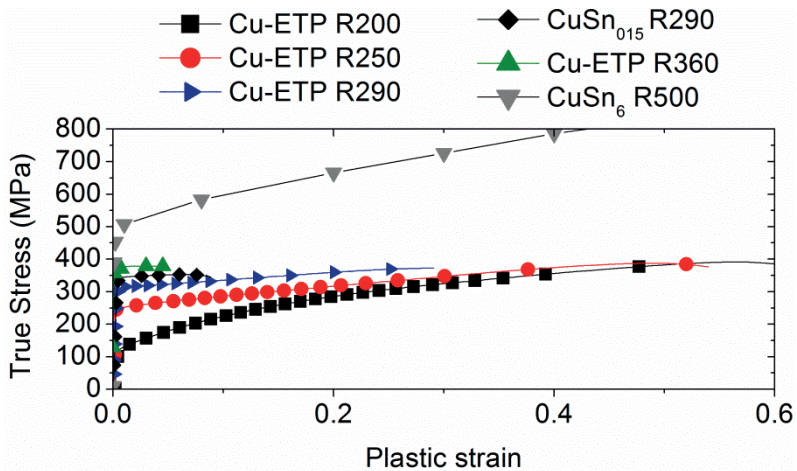


Figure 4.2: Overview of flow curves for different bulk materials along the rolling direction.

The hardest materials showed a slight difference between the flow curves in the two different directions of the sheet. Nevertheless, sensitivity analyses in the simulation model showed that this difference does not affect the course of the F_I - x_I curve, and its effect on the absolute insertion values is negligible in comparison to the effect of the friction law.

Texture analyses were also carried out in sheet materials. Despite the rolling texture present on the hardest samples, no tension-compression anisotropy can be measured due to the nature of the probes.

Thus, the material data presented in Figure 4.2 will describe the plastic behavior of copper sheets.

Tensile and compression tests in bars

The copper bars used to produce the male components in *configuration A* were characterized both thorough tensile and compression tests.

Tensile tests were carried out analogously to the test in sheet materials. Compression tests were performed according to DIN 50106 norm.

Both tests delivered different results, as revealed in Figure 4.3.

The different behavior of the material under tensile and compressive load can not be explained by the Bauschinger effect, since the tension-compression anisotropy takes place in this case for a broad range of strains instead of just affecting the yield stress [Rös12].

Thus, this tension-compression anisotropy can only be attributed to the material's anisotropy and texture.

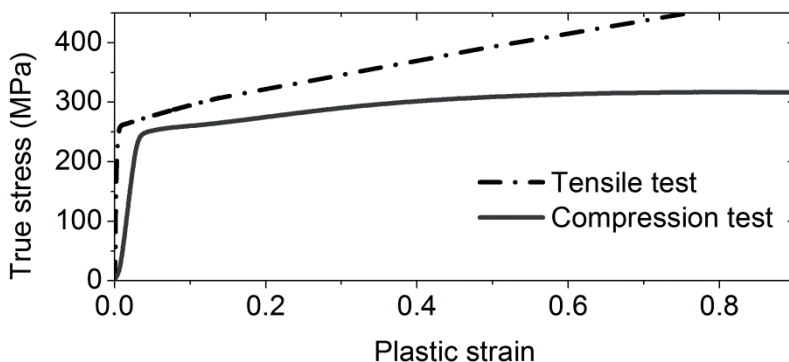


Figure 4.3: Tensile vs. compression tests for Cu-ETP R250 bars.

Electron-Backscatter-Diffraction (EBSD) measurements were carried out, in order to assess the texture in the copper bars. A dual beam Focused Ion Beam (FIB) was used (Zeiss Auriga 60, detector DigiView). Samples were grinded and electro-polished, in order to reduce preparation induced deformations (see preparation methods in *Appendix A*).

Between 34 000 and 35 000 measurements compose each EBSD scan presented in this chapter, and a $1.5\ \mu\text{m}$ step size was chosen. A grain dilation and Confidence-Index (CI) standardization were applied as cleanup procedures, being 0.031 the worst case of data fraction modified after the cleanup. Harmonic Series Expansion was used as texture calculation method.

Figure 4.4 displays the tensile texture present in the bars [Böh03, Len55, Yap07]. This texture is also observable in the inverse pole figure in Figure 4.5.

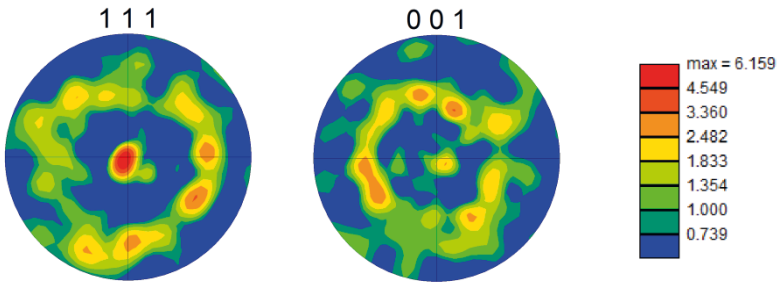


Figure 4.4: Texture measurements for a Cu-ETP R250 bar: Pole figures. The axis of the Cu bar is perpendicular to the figure's plane, and the measurements were carried out in the middle of the copper bar. The contours represent the texture intensity in arbitrary units.

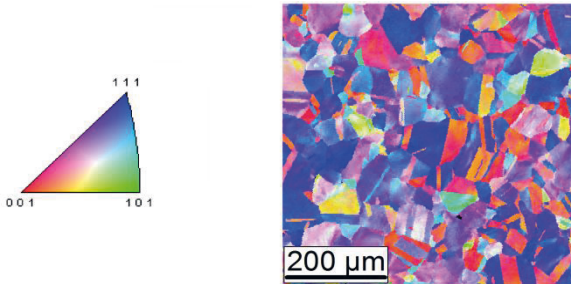


Figure 4.5: Texture measurements for a Cu-ETP R250 bar: Inverse pole figure. The axis of the Cu bar is perpendicular to the figure's plane, and the measurements were carried out in the middle of the copper bar.

The uniaxial tension on the cold-worked bars forms invariably fiber textures, which are often represented as inverse pole figures. After tension of fcc materials, the textures can be described by two fibers with $\langle 111 \rangle$ and $\langle 100 \rangle$ parallel to the deformation axis. This phenomenon has already been measured for copper bars [Naa87]. The relative proportion of the two fibers may vary with initial texture, deformation mode, and the Staking-Fault-Energy (SFE) [Eng10]. Figure 4.4 confirms this distinct fiber texture on the bars.

The effect of this texture and the anisotropic behavior displayed in Figure 4.3, will be assessed in the cold-joining simulation in the following section.

4.2.3 Implementation of the material data

Characterization of sheet materials

The CJPes of *configuration B* components will be used to assess the obtained material description in copper sheets, since both contact partners are in this configuration die-cut from a copper sheet.

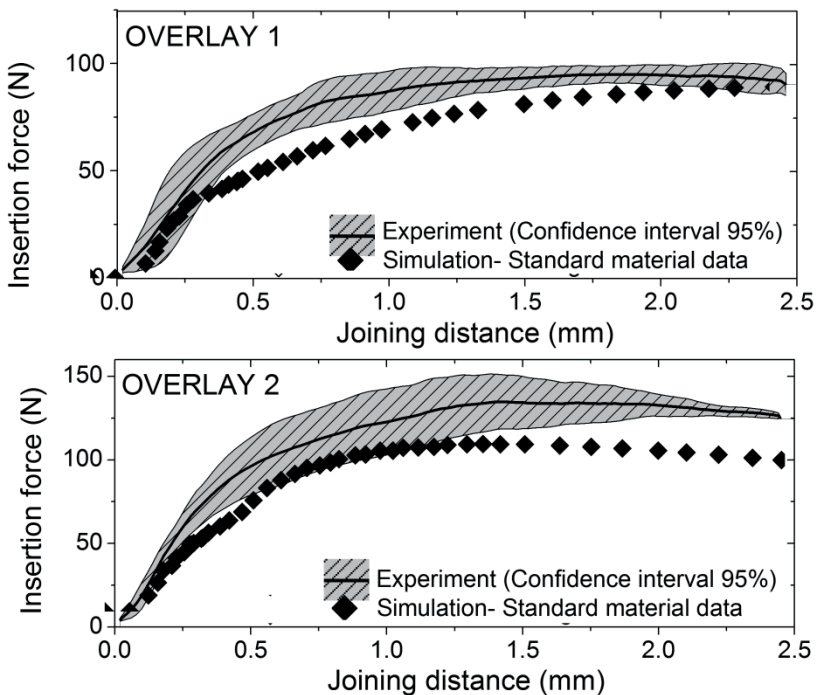


Figure 4.6: Cold-joining simulation of a *case 1* material combination Cu-ETP R200/ Cu-ETP R200 in *configuration B*. Components were joined in delivery condition.

From Figure 4.6 to Figure 4.11, the flow curves revealed in section 4.2 are implemented in the cold-joining simulation.

The results are classified, analogously to *Chapter 3*, in *case 1*, *case 3*, and *case 4*.

Each case is assessed in two different geometries (overlay 2 is larger than overlay 1) and two different lubrication situations, since a single material law, should be able to describe the CJP under all these circumstances.

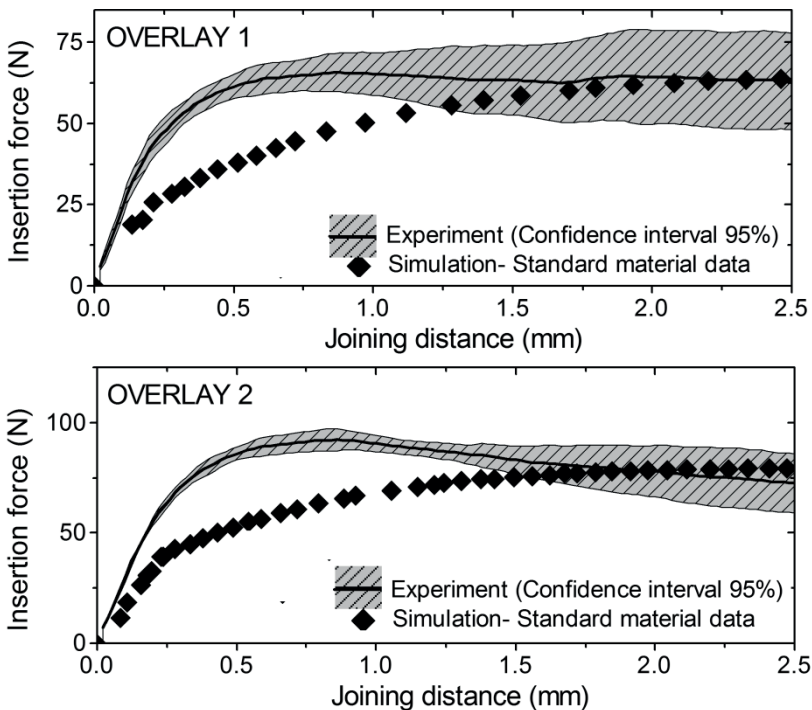


Figure 4.7: Cold-joining simulation of a *case 1* material combination Cu-ETP R200/ Cu-ETP R200 in *configuration B*. Components were joined after relubrication.

Figure 4.6 and Figure 4.7 show, that the standard material law, does not exactly represent the experimental F_I - x_I progressions, for the *case 1* CJP.

This is due to the processes that significantly strengthen the soft Cu-ETP R200 material during the production of the component. That is why, the material data determined in the bulk material can not describe the component correctly.

Approaches for a better simulation of the *case 1* CJPs are presented in the two following sections.

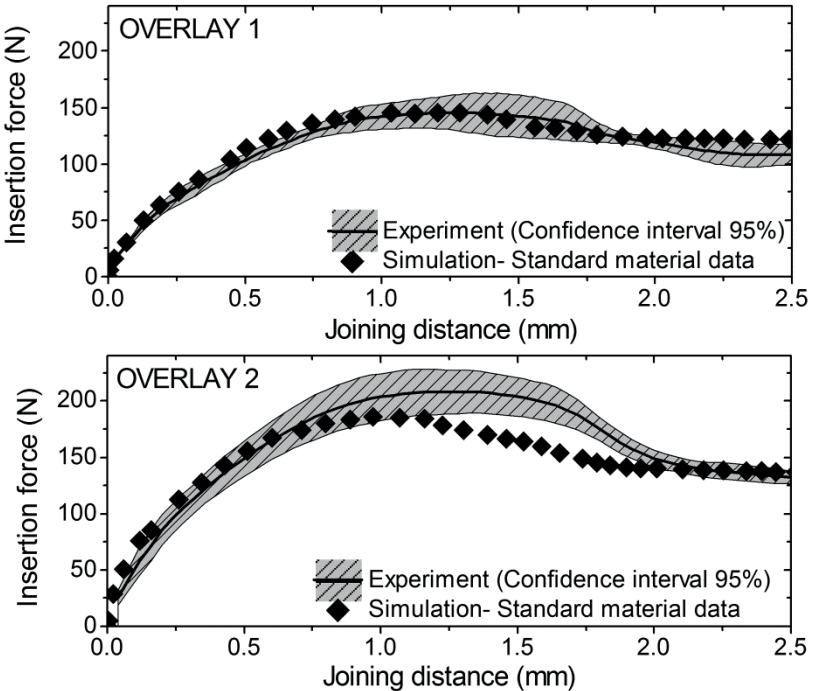


Figure 4.8: Cold-joining simulation of a *case 3* material combination CuSn₆ R500 (pin)/ Cu-ETP R200 (plate) in *configuration B*. Components were joined in delivery condition.

Figure 4.8 and Figure 4.9 on the contrary, exhibit a fairly accurate description of the *case 3* CJPes.

The difference in strength between both components is so high in this case, that no process on the bulk material affects the relative strength between them.

Thus, the bulk material data is sufficient to describe which component will deform the other one first.

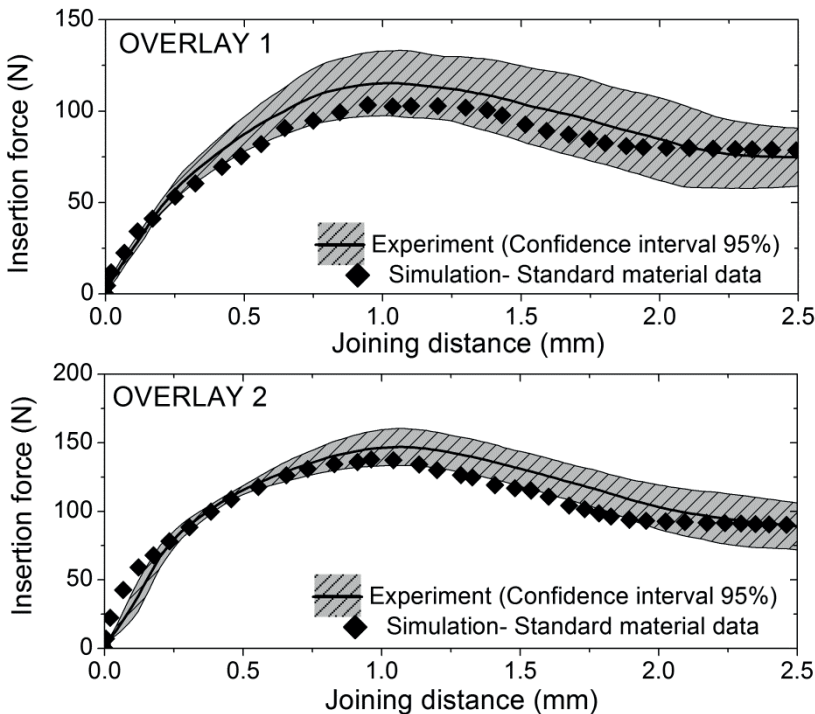


Figure 4.9: Cold-joining simulation of a *case 3* material combination CuSn₆ R500 (pin)/ Cu-ETP R200 (plate) in *configuration B*. Components were joined after relubrication.

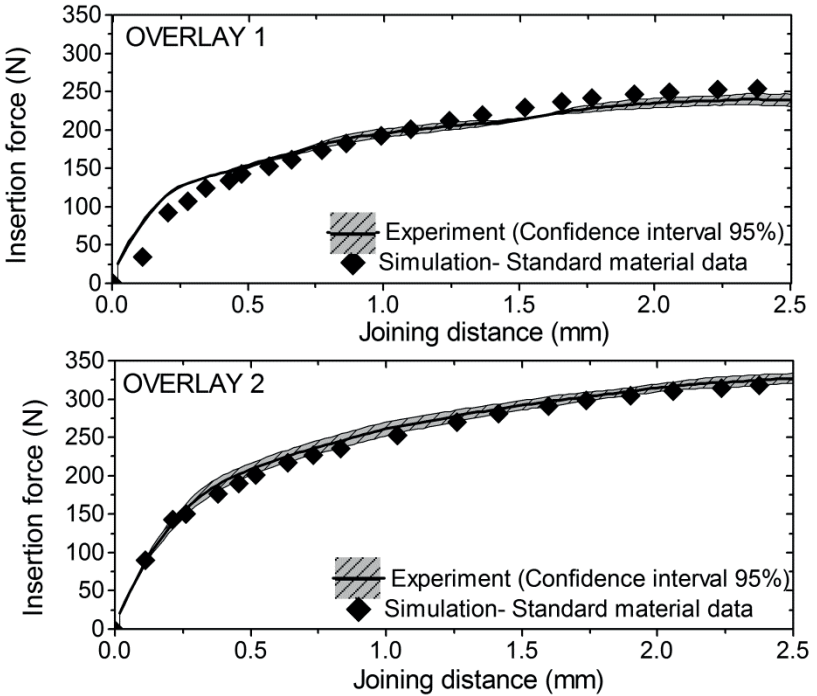


Figure 4.10: Cold-joining simulation of a *case 4* material combination CuSn₆ R500/ CuSn₆ R500 in *configuration B*. Components were joined in delivery condition.

Figure 4.10 and Figure 4.11 correspond to *case 4* CJPs.

In this case, the description of the CJP for the components in delivery condition is very precise (Figure 4.10). Nonetheless, this accuracy deteriorates for relubricated parts, that is to say, for lower friction coefficients.

This phenomenon was to be expected. On the one hand, the harder material compared to *case 1* minimizes the effect that the production processes have on the strength of the components. On the other hand, this effect is more visible for low friction

coefficients, where a much higher proportion of the forces in the F_I-x_I curves are used to plastically deform the components and not dissipated as friction.

The conclusion that can be drawn from this sections is, that those CJPes whose components have not gone through a change on their relative strength during their production process, can be simulated with material data obtained through tensile tests in bulk material.

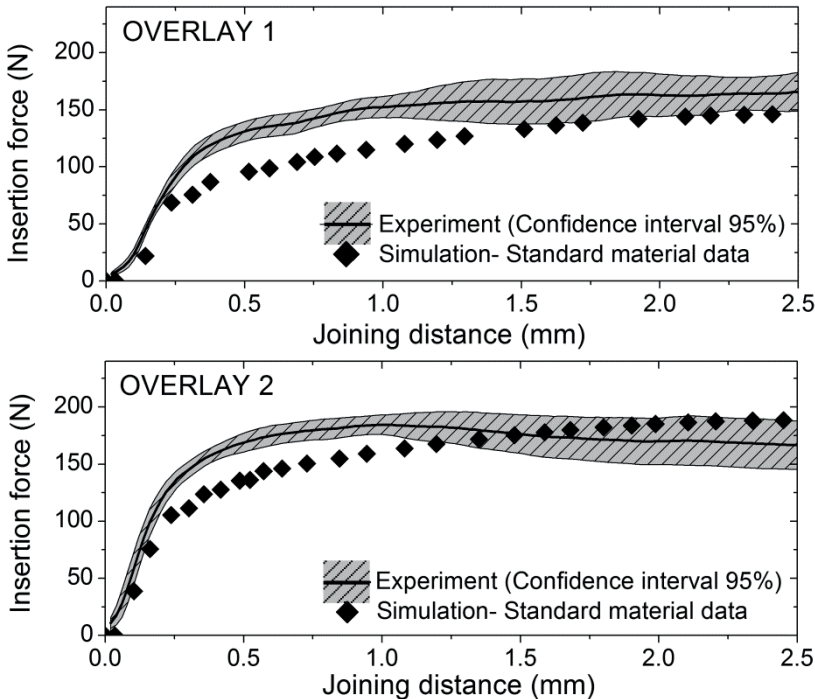


Figure 4.11: Cold-joining simulation of a *case 4* material combination CuSn_6 R500/ CuSn_6 R500 in *configuration B*. Components were joined after relubrication.

Alternative methods for the cases that cannot be described with the standard material description presented in this section, are proposed in section 4.3 and 4.4.

Characterization of bars

Figure 4.12 reveals the effect of applying each of the two different flow curves in Figure 4.3 on the cold-joining simulation.

The flow curve corresponding to the compression test offers a better description of the CJP. The compression tests resembles more accurately the stress state during cold-joining than the uniaxial tension.

Figure 4.4 and Figure 4.5 confirmed the fiber tensile texture, and thus, the anisotropy present in the copper bars.

Figure 4.13 shows the stress state of the copper bar during cold-joining, and how the compression stress prevails. That is why the compression test offers a far more accurate description of the material behavior of cold-drawn components.

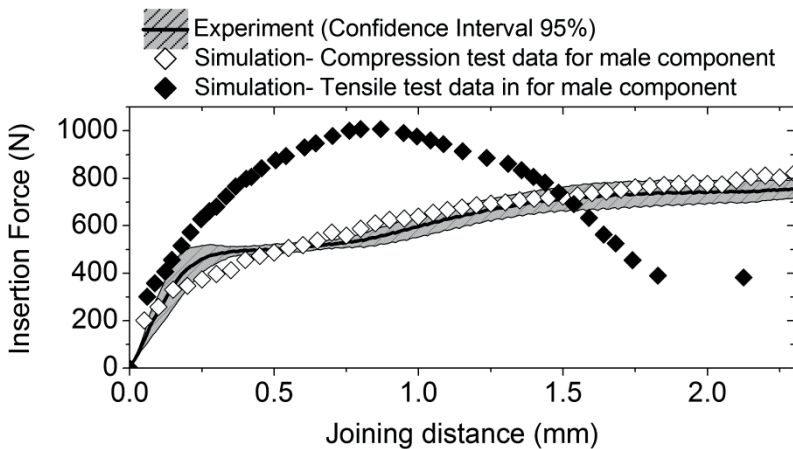


Figure 4.12: Effect of the consideration of tension-compression anisotropy on the cold-joining simulation on a *configuration A* simulation.

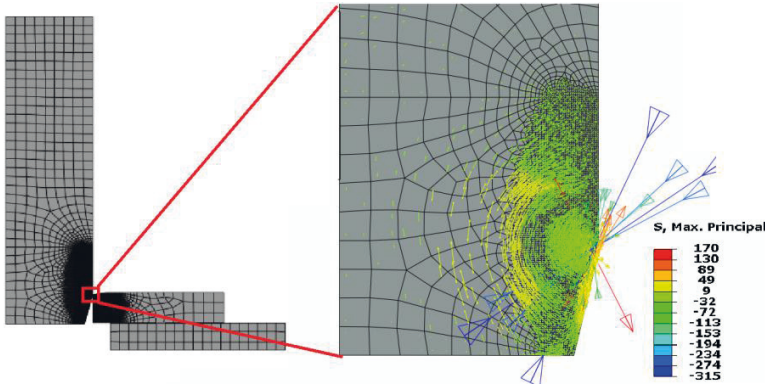


Figure 4.13: Strain state of the copper bar during the CJP of a *configuration A* connector. Stresses are represented in MPa.

The results in Figure 4.12 show, that the anisotropic behavior of cold-drawn copper components has to be regarded in the FE simulation of CJPEs. Nevertheless, the simulation with the material data obtained under a similar stress situation to the CJP, delivered a correct representation of the experiments, without the need of an anisotropic material description in the model.

4.3 New method 1: Small-punch tests

Results in section 4.2 point out the necessity of determining material data in-situ in the copper piece, since the bulk material properties significantly change during the production process of some components. Therefore, an improved description of the *case 1* CJPEs is pursued in this section.

Small-punched tests are used in combination with optimization algorithms to indentify plastic deformation and failure properties of ductile materials [Abe03, Mar96, Ngu00].

This section presents small-punch tests as an alternative to the standard material characterization methods presented in section

4.2., since this method enables the material characterization directly on the components.

4.3.1 Methodology

The methodology for the determination of material properties by means of a small-punch test is represented in Figure 4.14.

The procedure is based on the comparison of a compression test with a punch with its FE simulation. The material data of the simulation is iteratively modified in order to match the F-x progression of the experiment.

A bilinear flow curve parameterization was applied to all materials, except to the material Cu-ETP R200, which needed an exponential parameterization, due to its flow behavior.

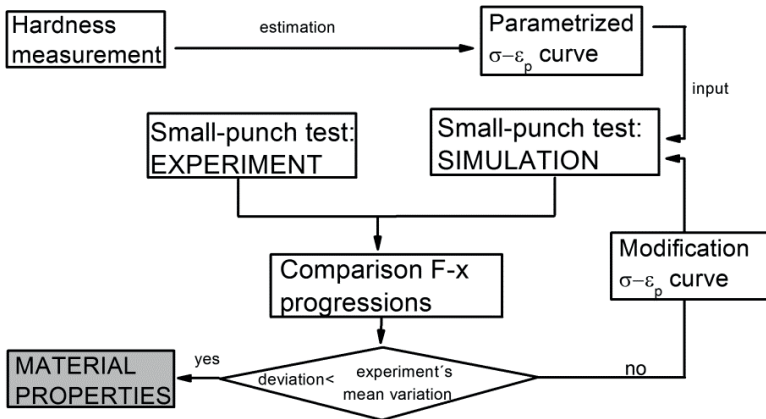


Figure 4.14: Schematic representation of the procedure for the material data determination by means of small-punch tests.

Experiments

For an experiment in order to be suitable for the determination of material properties, it has to be independent of other variables, such as friction and boundary conditions.

Therefore, the experiments were carried out with lubricated and dry surfaces, to assess the effect of the friction.

The friction coefficient, proved not to affect the F-x progression of the experiments.

The boundary conditions of the experimental setup were optimized, in order to minimize disturbance factors.

The material data is validated by means of several small-punch tests with different punch geometries (Figure 4.15-left).

Since the experiments are just dependent on the material data, they are seen as appropriate to adjust material laws according to them.

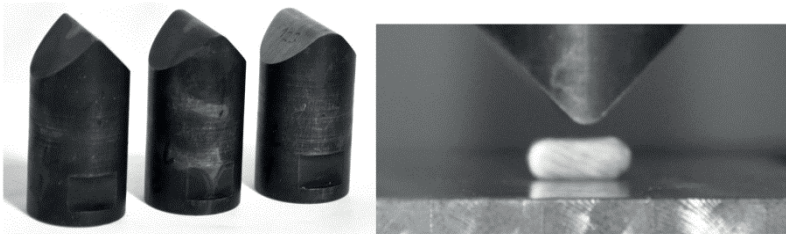


Figure 4.15: Left: different punch geometries. The curvature of the punch's tip was varied from a 1mm to a 5 mm radius. Right: copper component before being subjected to a small-punch test.

Simulation

A simulation model of the small-punch test was built. The requirement on the simulation model, as well as on the

experiment, is having the material data as the only input parameter that affects the F-x progressions.

The simulation results showed no sensitivity to the boundary conditions.

However, the F-x progressions are affected by the friction coefficient chosen for the simulation. Therefore, the used friction coefficient between the components and the punch has to be validated.

4.3.2 Validation

To validate the friction coefficient used as input for the simulation model, the deformation of the component was compared between the experiment and the simulation.

Figure 4.16 represents the approach used for the election of friction coefficient. This parameter strongly affects the pile up geometry produced by the punch, and was fitted to match the real geometry observed in the experiments.

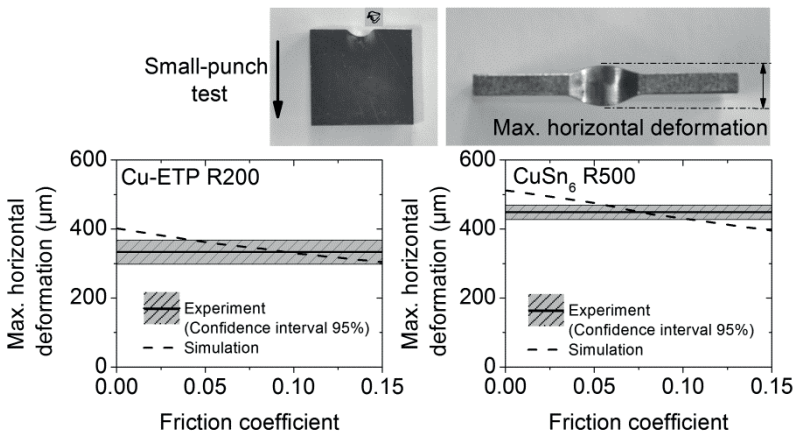


Figure 4.16: Validation of the friction coefficients used for the small-punch test simulation.

For all materials and lubrication situations analyzed, the friction coefficients are between 0.06 and 0.09.

4.3.3 Results

Characterization of bulk materials

Small punch tests were carried out in all sheet materials. Figure 4.17 represents the characteristic results obtained for bulk materials. The first simulations carried out with the material data obtained through tensile tests, were able to describe the experiments without any optimization.

Thus, the experiments just validated the tensile test results in all studied variants.

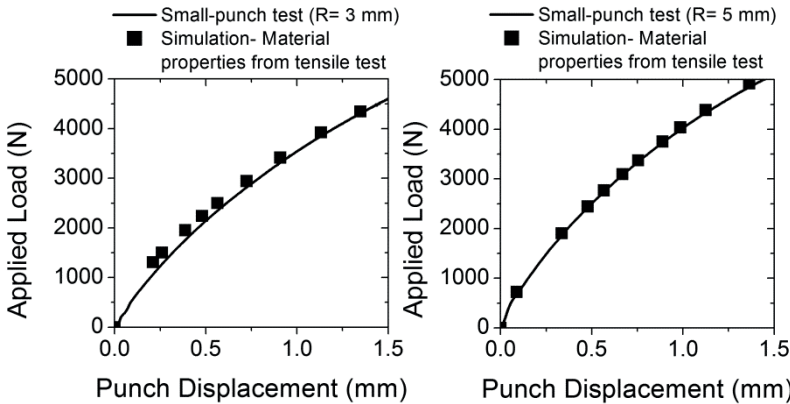


Figure 4.17: Results of the small-punch tests (for different punch geometries) on the Cu-ETP R200 bulk material, with the material data based on tensile tests.

Characterization of components

Not only bulk materials, but also components can be directly studied through small-punch tests.

In Figure 4.18 comes into view that the bulk material data is not suitable anymore for the characterization of a component, due to the strengthening that takes place during its production process. Figure 4.18 is the most representative case for this strengthening effect, since the softest material was die-cut to form a small component (*configuration B* pin Cu-ETP R200).

Therefore, the strength in the material model has been accordingly adjusted to match the experiments, as displayed in Figure 4.14. The effect of adjusting the material data is assessed below.

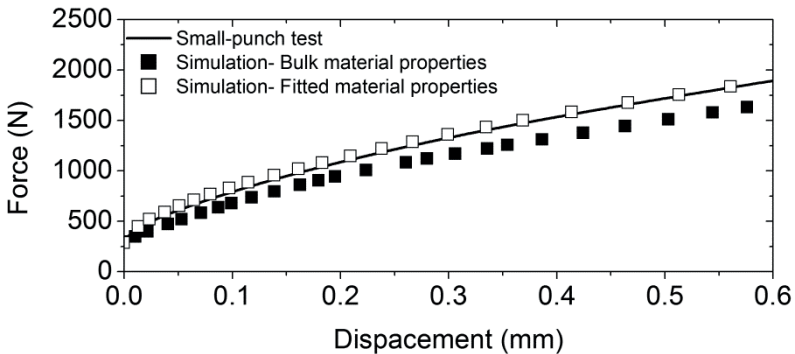


Figure 4.18: Adjustment of the material data for the small-punch test on the Cu-ETP R200 *configuration B* pin.

Impact on the force-fitting simulation

In section 4.2 was revealed that the standard material law is not able to describe the *case 1* CJPEs. This is due to the ductile nature of Cu-ETP R200, which has been strengthened during die-cutting.

The same effect is visible in the small punch test presented in Figure 4.18.

Therefore, the effect of the adjusted material law is assessed on the cold-joining simulation (Figure 4.19).

No significant improvement of the F_I - x_I progression's prediction is observable in Figure 4.19. This fact, points to the non homogeneous strengthening of the components, which cannot be modeled by simply upscaling the bulk material's flow curve.

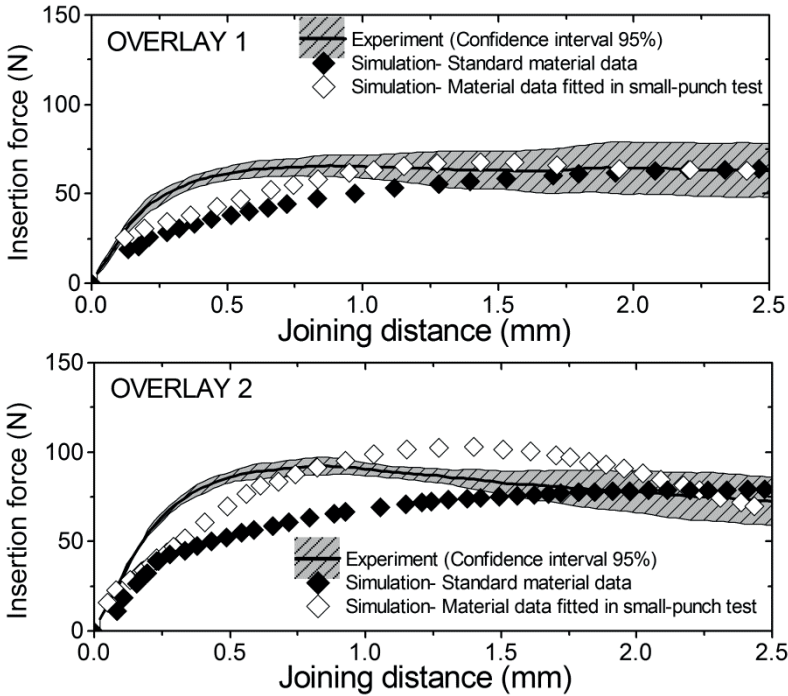


Figure 4.19: Impact of the fitted material description (small-punch test) vs. the standard material description on the cold-joining simulation of material combination Cu-ETP R200/ Cu-ETP R200 in *configuration B*. Components were joined in delivery condition.

4.3.4 Summary

The small punch tests proved to be a valid method for the determination of flow curves for bulk materials. This method represents thus a cost-effective alternative for the determination and validation of material properties for a wide range of plastic strains.

The tests underpinned the validity of the tensile tests for the characterization of sheet bulk materials.

Small-punch tests on small die-cut components showed on the contrary, that the strengthening of the material during their production process requires an accordingly harder material law.

The material law for these components was iteratively optimized to adjust it to the results of the small-punch test. This modified material law was applied on the cold-joining simulation, pursuing an improvement on the simulation of joining processes such as *case 1*, where tensile test proved in section 4.2 not to be able to describe the components.

However, the modified material law does not improve the predictability of the CJP' simulation.

This fact can be traced back to the inhomogeneous nature of the component's strengthening during die-cutting. An average upscaling of the bulk material's flow curve is not able to describe the strength distribution in such a component.

Therefore, a method for the description of inhomogeneities at punched edges is presented in the following section.

4.4 New method 2: Local material characterization

Methods for the in situ determination of material properties in the components have already been applied for elastic solderless connectors (press-fit connectors) [Man07].

The components for the massive CJT go also through a strength hardening during their production process. Moreover, die-cutting produces a gradient of hardness at the punched edge.

Nanoindentation has already been used to quantify strain inhomogeneity of formed products [Pet03]. Nevertheless, the challenge of describing in a FE model the inhomogeneity at punched edges has not been addressed before. This section proposes a new method for this purpose.

4.4.1 Motivation and characterization of punched edges

Die-cutting is the preferred technology for a cost-efficient production of tightly tolerated massive copper components for the CJT.

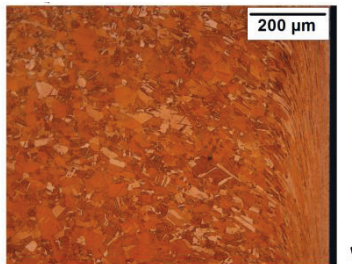


Figure 4.20: Microstructure at a Cu-ETP R200 punched edge. The punched edge and the stamping direction are marked by the arrow on the right hand side.

Strong changes in the copper microstructure due to die-cutting are observable under the light microscope (Figure 4.20).

Since two punched edges often form the contact area of the CJC, the exact determination of the material properties in this zone is essential.

The hardening mechanisms that take place during die-cutting are studied in this section and a new method is proposed to account for the increased yield strength at punched edges.

The two softest materials, Cu-ETP R200 and Cu-ETP R250, are studied in this chapter, due to their higher susceptibility to strength hardening.

Work hardening and grain boundary strengthening are the strengthening mechanisms that can take place due to die-cutting.

EBSD measurements were carried out to analyze both mechanisms. Probes were prepared analogously to the samples for the texture measurements in section 4.2 (see *Appendix A*).

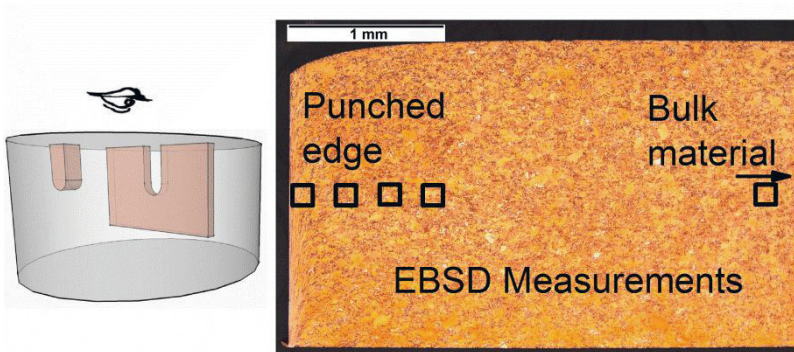


Figure 4.21: Schematic representation of the sample preparation and the position of the EBSD experiments.

The measurements were carried out analogously to the texture measurements in the bars, regarding measurement points and clean up procedures.

Both bulk materials were characterized and the corresponding punched edges were studied with higher resolution (Figure 4.21).

Grain Boundary Strengthening

Die-cutting produces a grain boundary strengthening of the copper. Figure 4.22 shows the distribution of grain size along the affected area.

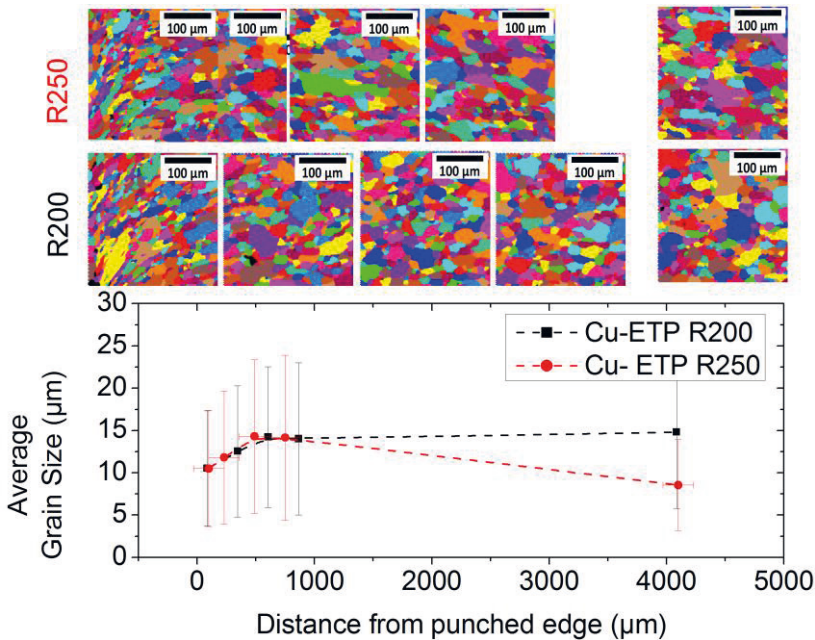


Figure 4.22: Grain size measurements at punched edges of plates with different bulk materials.

Each point in the graph represents the average grain size calculated from the corresponding picture. The error bars indicate the standard deviation of the grain size distribution.

Work hardening

Plastic deformation is the development, movement and multiplication of dislocations. If these movements and multiplications of dislocations are not able to relieve the whole stress applied to the material, rotations in the crystalline structure take place. These rotations are known as local misorientations and can be used to quantify the so called geometrically necessary dislocations in the crystalline structure [Eng00, Wri11].

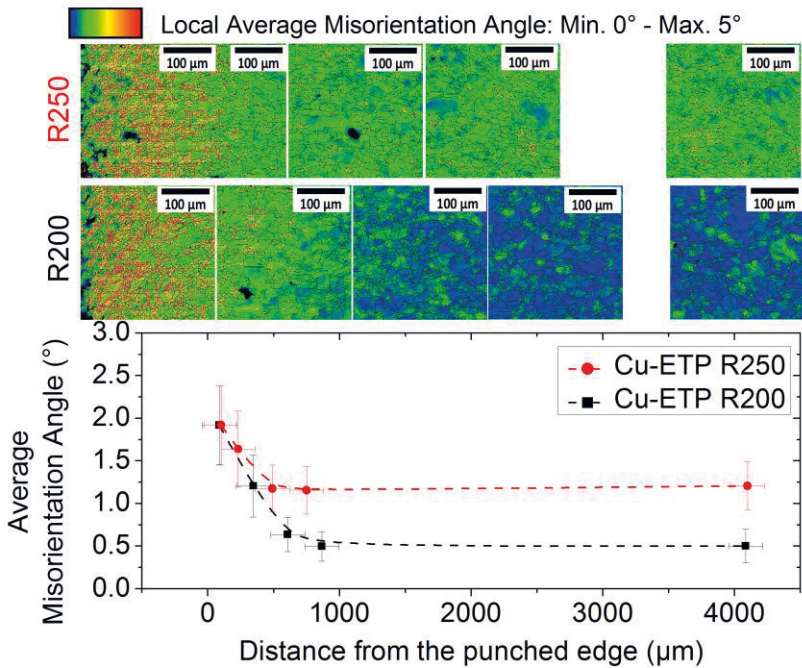


Figure 4.23: Local Average Misorientation Angle (KANM) at punched edges of plates with different bulk materials.

Figure 4.23 shows the devolution of the average misorientation angle from the punched edge to the bulk material. Each point in the graph represents the average misorientation angle of the corresponding picture. A kernel-based analysis method (KANM) has been applied, third order nearest neighbors were used, and 5° were considered the maximum misorientation.

The measurements (Figure 4.23) show that the influenced area due to die-cutting is larger than the altered zone noticeable under the light microscope (Figure 4.20). Die-cutting increased the amount of dislocations up to 1 mm from the edge. The strength difference between both bulk materials, obtained by means of a cold-rolling step, is also observable in terms of local average misorientation angle.

4.4.2 Methodology

A methodology will be proposed in this section to quantify the hardening mechanisms detected by the EBSD measurements and implement the description of this inhomogeneity at punched edges in a FE model.

Step 1: Hardness Screening of punched edges

Nanoindentation in an instrumented indentation equipment was chosen as reliable and accessible method to quantify the effects of both strengthening mechanisms on the flow characteristics of the material. Nanoindentation has already been widely used to characterize small volumina of material in work hardened areas with large hardness gradients [Ahn00, Nob04, Pet03, Son07].

Most procedures use continuous ball indentation to determine the stress-strain behavior of materials, as it delivers information about the complete flow curve of the material with a single indentation [Anh01, Biw94, Hil89]. Nonetheless, a Vickers indenter was used for the characterization of work hardened

zones, due to the small indentation sizes needed in order to characterize high hardness gradients in small work-hardened zones.

Analogously to the previous section, the hardness screening is going to be applied on the Cu-ETP R200 and Cu-ETP R250 materials, because of their ductility and sensitivity to strength hardening. The punched edges in both materials are going to be studied in the two different geometries (pin and plate) of the *configuration B* CPCs.

Samples were grinded and polished up to a 1 μm diamond suspension, before a vibratory polishing with colloidal suspension during 4 hours. The parameters of the nanoindentation for the investigation using a Fisherscope HM2000 were chosen according to the norms DIN EN ISO 6507 and DIN EN ISO 14577 and thoroughly discussed in [Ari12].

The Two-Dimensional (2D) hardness mappings were carried out in cross-sections. The One-Dimensional (1D) hardness distributions are a simplified representation of the 2D measurements as represented in Figure 4.24.

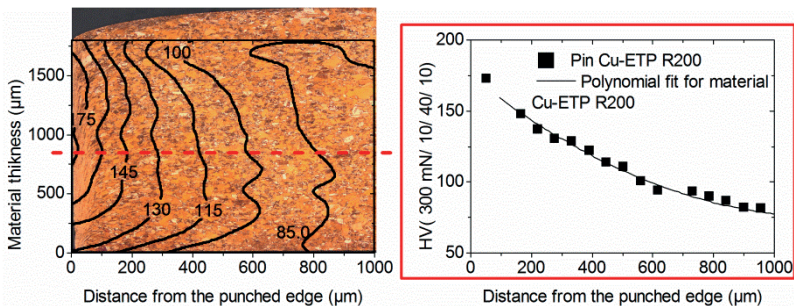


Figure 4.24: Schematic representation of the nanoindentation experiments and their simplifications. Samples were embedded as shown in Figure 4.21.

Step 2: Correlation between hardness and flow curves

Not only the hardness characterization of the work hardened zones, but also a correlation between hardness and flow characteristics is needed in order to get an inhomogeneous material law for the FE simulation of CJPs.

The correlation between hardness and flow characteristic of metallic materials is well known [Tab51, Sun94]. Several analytical approaches and FE simulations have been suggested to correlate effective strain with hardness.

The correlation between hardness and flow curves was experimentally determined for a better accuracy. For this purpose, flow curves and hardness were measured on Cu-ETP cold-rolled sheets with different hardness specifications.

The flow curves for different Cu-ETP materials (some of them already presented in section 4.2) will set up the basis for the correlation of hardness values to flow characteristics. The samples cover the whole spectrum of hardness available for Cu-ETP.

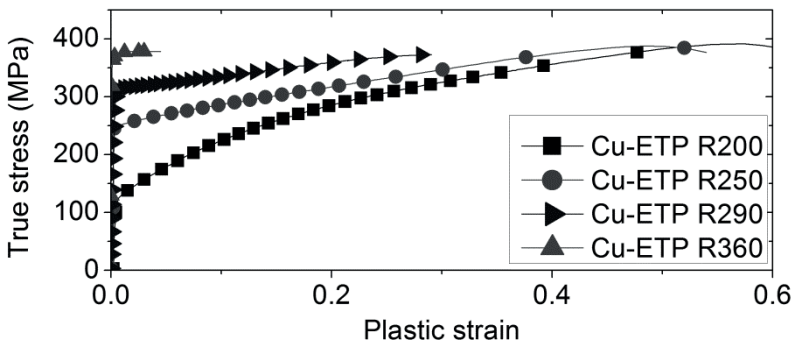


Figure 4.25: Flow curves for Cu-ETP samples with different hardness values.

The hardness of the different bulk materials was examined in identical conditions to the hardness characterization of the punched edges. In Figure 4.26 a characteristic hardness value is attributed to each flow curve presented in Figure 4.25.

A linearly interpolated flow curve between the two corresponding flow curves in Figure 4.25 will be assigned to any hardness between two characteristic hardness values in Figure 4.26.

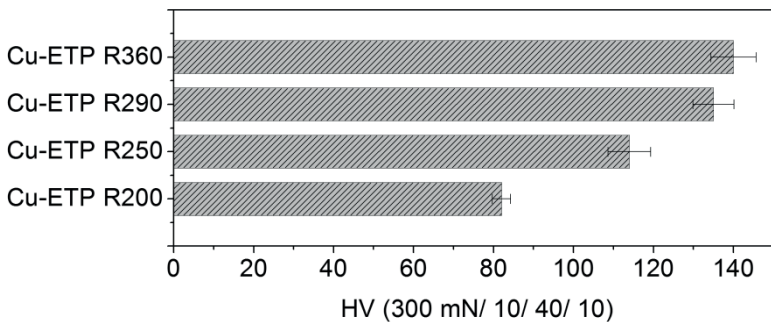


Figure 4.26: Characteristic hardness of Cu-ETP Samples.

Step 3: Implementation in a Finite Element Simulation

A hardness value characterizes every element of the FE mesh in the influence area of the die-cutting.

In the case of 2D hardness screenings, an algorithm was developed to assign to every integration point in the mesh, an interpolated value of hardness between the closest existing nanoindentation measurements.

If a 1D hardness distribution is implemented, an analytical function describes the hardness distribution from the punched edge to the bulk material.

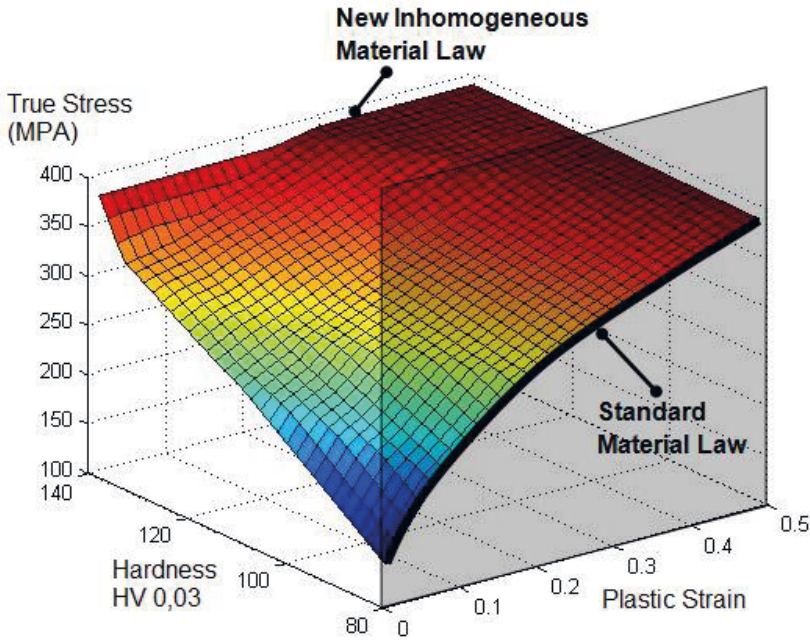


Figure 4.27: New inhomogeneous (hardness dependent) material law vs. the standard flow curve for Cu-ETP R200 bulk material.

A hardness dependent material law assigns to every element, the corresponding flow curve interpolated between the curves in Figure 4.25.

Figure 4.27 represents the new hardness dependent material law. This material law will be applied for components that have been die-cut from the Cu-ETP R200 bulk material, since this soft material undergoes the most significant changes in strength during die-cutting.

4.4.3 Validation

A small punch test (introduced in section 4.3) was carried out on a formed part to validate the new inhomogeneous material law.

The material data obtained from a tensile test (Figure 4.25, flow curve Cu-ETP R200) delivered a very good agreement between experiment and simulation on bulk material, as already presented in section 4.3.

Nonetheless, at the punched edge the bulk material data underestimates the experimental forces needed to deform the part.

The most significant example is shown in Figure 4.28, since the softest bulk material was tested in the smallest component geometry, where 2 mm out of 4 mm are under the effect of the material strengthening due to die-cutting.

The implementation of the new inhomogeneous material data in this case shows a significant improvement on the agreement between simulation and experiment.

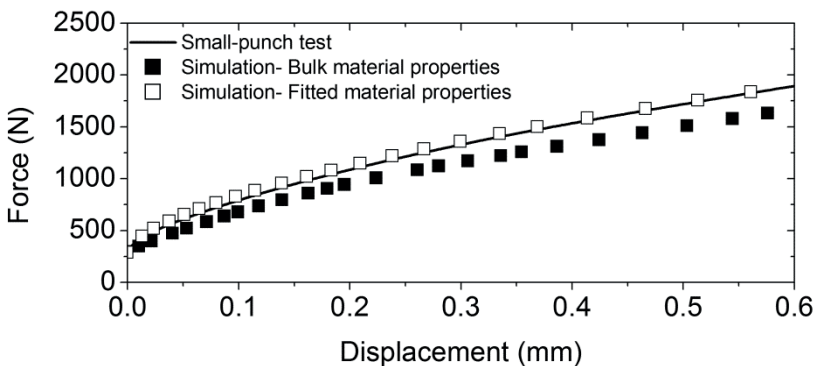


Figure 4.28: Results of a small-punch test on a *configuration B* Cu-ETP R200 pin: comparison between standard and inhomogeneous material law.

Thus, the new inhomogeneous material law is validated.

Furthermore, no difference between the 2D and 1D inhomogeneity descriptions is to be seen in Figure 4.28, which also validates the use of simplified 1D hardness distributions.

4.4.4 Results

This section compiles the main results of the characterization of punched edges, and the impact of applying this inhomogeneous description in the FE simulation of the CJPes.

Hardness distribution at punched edges

From Figure 4.29 to Figure 4.32 the changes in hardness produced by the die-cutting process are represented for different bulk materials and geometries.

A major material strengthening was revealed at punched edges. Die-cutting induces hardness values twice as high as in bulk material.

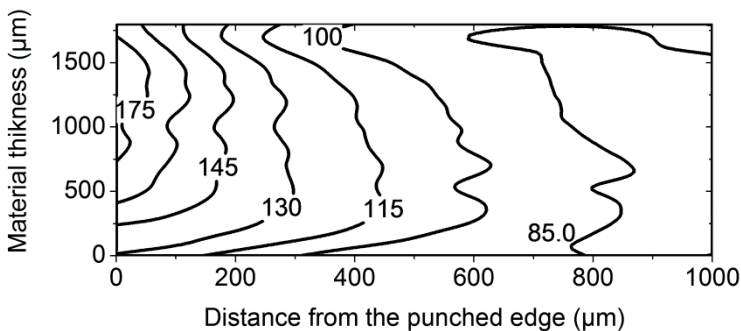


Figure 4.29: Two dimensional hardness screening at a punch edge of a *configuration B* Cu-ETP R200 pin. The numbers represent the hardness values in HV (0.3/ 10/ 40/ 10).

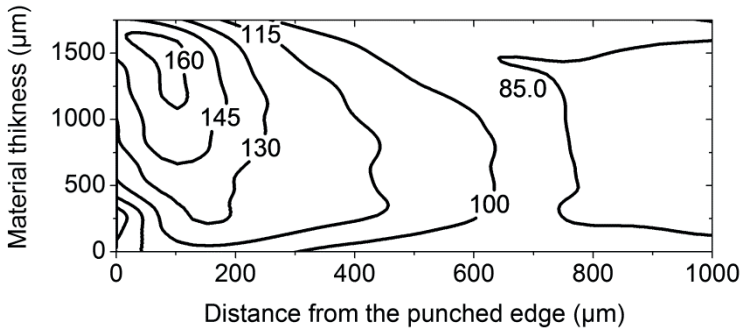


Figure 4.30: Two dimensional hardness screening at a punch edge of a *configuration B* Cu-E1P R200 plate. The numbers represent the hardness values in HV (0.3/ 10/ 40/ 10).

The influence zone reaches, as expected from the EBSD experiments, up to 1 mm from the edge, which proves nanoindentation to be a suitable method to account for the work-hardening at punched edges.

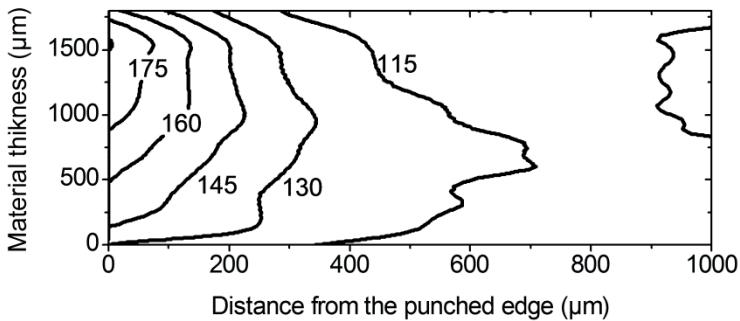


Figure 4.31: Two dimensional hardness screening at a punch edge of a *configuration B* Cu-E1P R250 pin. The numbers represent the hardness values in HV (0.3/ 10/ 40/ 10).

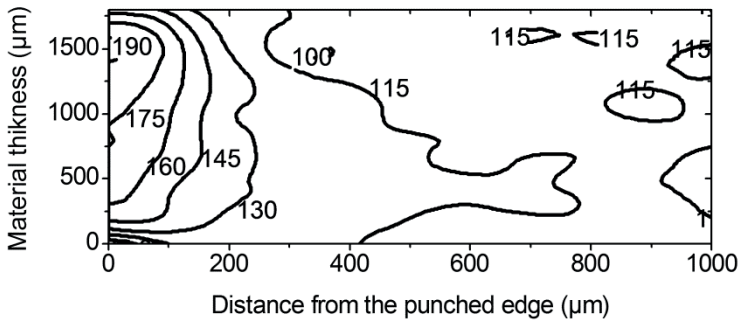


Figure 4.32: Two dimensional hardness screening at a punch edge of a *configuration B* Cu-ETP R250 plate. The numbers represent the hardness values in HV (0.3/ 10/ 40/ 10).

The implementation of two dimensional hardness distributions in fine FE meshes requires time consuming interpolation algorithms and slows down the FE simulations. Therefore, a one dimensional simplification of the hardness distribution is pursued.

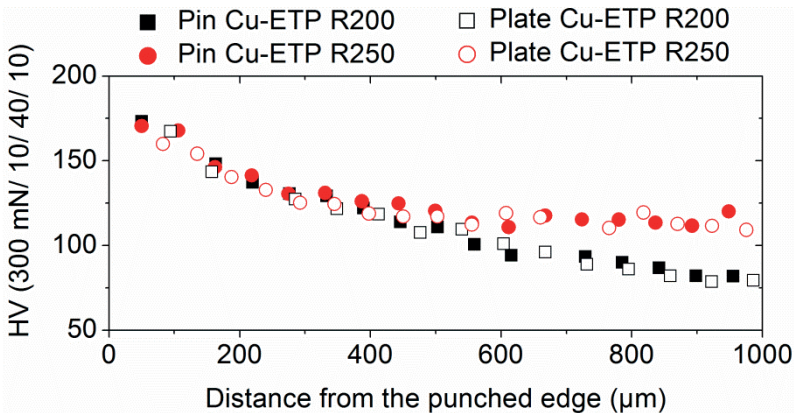


Figure 4.33: One dimensional simplification of the hardness screenings in Figure 4.29 to Figure 4.32.

Figure 4.33 represents a simplification of the measurements from Figure 4.29 to Figure 4.32. The hardness distribution in the middle of the copper sheet is plotted as indicated in Figure 4.24. This simplification does not exactly correspond to the more realistic 2D description, since the isolines from Figure 4.29 to Figure 4.32 are not vertical. The effect of this simplification has proved to have no noteworthy effect on the small punch tests carried out for the validation of the methodology in Figure 4.28.

Figure 4.33 reveals a hardness distribution produced by die-cutting, which is virtually independent of the component's geometry, if the die-cutting parameters (such as the clearance) are kept constant.

The hardness evolutions can even be considered independent of the bulk material, except the corresponding discrepancy in the bulk material's hardness to which the curves converge.

Moreover, the distributions can be fitted with a polynomial function as represented in Figure 4.34.

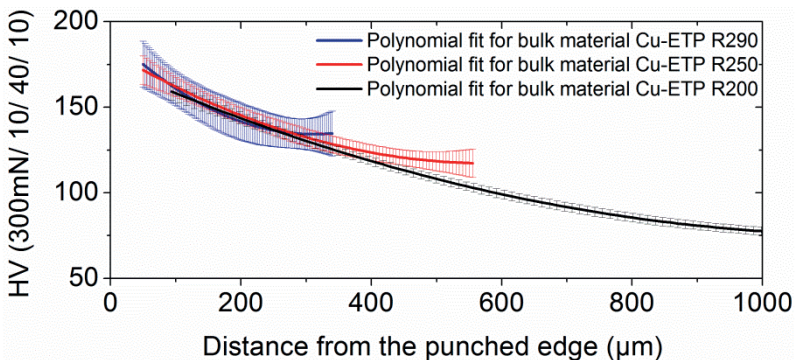


Figure 4.34: Polynomial description of the hardness distribution at punched edges for different bulk materials.

The 1D simplification and the polynomial fitting allow describing the influence of die-cutting with an analytical function. This simplification enables the implementation of hardness data on the mesh of the FE model without any interpolation algorithm. Besides, the convergence behavior of the FE simulation improves with an analytical description of the hardness distribution, since discontinuities in material stiffness would lead to poor convergence.

The polynomial description of the punched edges for each bulk material proposed in Figure 4.34 is also presented in equations (4.4) to (4.6), so that a hardness distribution can be applied in the FE mesh independently of the geometry where the edge is stamped and without the need of any experiment.

For bulk material Cu-ETP R200:

$$HV=7.12e-5 \cdot x_d^2 - 0.168 \cdot x_d + 174 \quad (4.4)$$

For bulk material Cu-ETP R250:

$$HV=1.93 \cdot 4 \cdot x_d^2 - 0.225 \cdot x_d + 182 \quad (4.5)$$

For bulk material ETP R290:

$$HV=5.99e-4 \cdot x_d^2 - 0.373 \cdot x_d + 192 \quad (4.6)$$

Impact on the force-fitting simulation

Beyond the validation of the new material law in a small punch test, the positive influence of the inhomogeneous material description has to be proved in the FE simulation of CJPes.

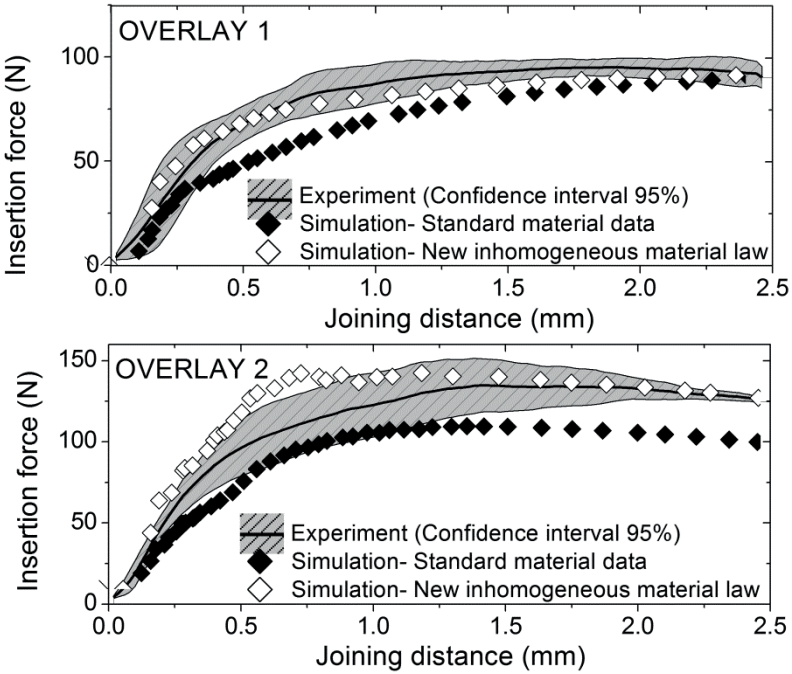


Figure 4.35: Impact of the inhomogeneous material description vs. the standard material description on the cold-joining simulation of material combination Cu-ETP R200/ Cu-ETP R200 in *configuration B*. Components were joined in delivery condition.

This improvement is assessed in Figure 4.35, where the inhomogeneous material law describes the F_I - x_I progressions significantly better. Furthermore, the new material law is able to describe the end joining force in the whole spectrum of overlays, with the same friction coefficient, which is fundamental for geometry comparisons.

The same improvement on the prediction of the CJP is displayed in Figure 4.36 for relubricated samples, which proves that the material description is valid for different friction coefficients.

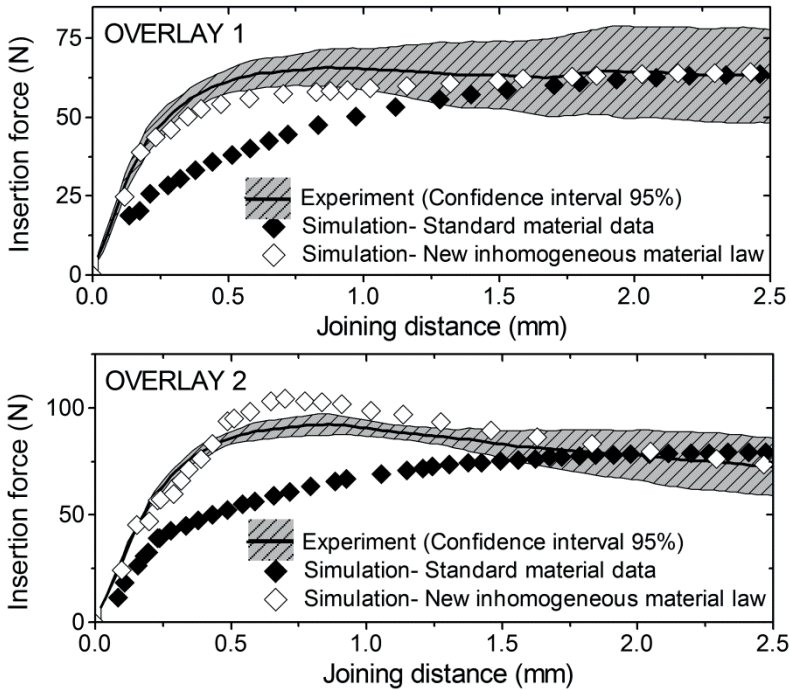


Figure 4.36: Impact of the inhomogeneous material description vs. the standard material description on the cold-joining simulation of material combination Cu-ETP R200/ Cu-ETP R200 in *configuration B*. Components were joined after relubrication.

The slight overestimation of the maximum joining forces for the bigger overlays is due to the 1D simplification of the hardness gradients. The polynomial description of the hardness devolutions assumes that the isolines of the 2D hardness screenings are vertical. This simplification leads to an overestimation of hardness values, and thus to a slightly overestimated material stiffness in the contact area.

4.4.5 Summary

The new inhomogeneous material law describes appropriately those CJPs, that the standard material description (section 4.2) and the fitted material law (section 4.3) could not predict.

The need of an inhomogeneous material law becomes clear for those material combinations, where the stamping of the components can alter the relative strength between them (*case 1*).

This improved material law proved to be valid for different geometries (overlays) and different frictional situations.

4.5 Summary

Chapter 4 shows the importance of a correct material characterization for the predictability of a CJP's simulation.

As introduced in *Chapter 1*, material properties for high plastic deformations are determined, the stress situation in the parts during the CJP is considered, and the components are characterized at the end of their production process.

The anisotropy and texture of bars has to be contemplated. However, just determining the material data in a similar stress state to the occurring in the CJP delivers good results.

Small punch tests proved to be a suitable alternative to tensile tests for the determination of flow curves. Nevertheless, the fitting of the material data by means of a small-punch test directly on the components, is not able to describe the strength distribution inside the die-cut pieces.

Table 4.2: Overview of required material descriptions for a good agreement between simulated and experimental F-x progressions.

		Female component	
		Cu-ETP R200	CuSn ₆ R500
Male component	Cu-ETP R200	<p>CASE 1: <u>Delivery condition:</u> Inhomogeneous material law required <u>Relubricated:</u> Inhomogeneous material law required</p>	<p>CASE 2: Chip formation</p>
	CuSn ₆ R500	<p>CASE 3: <u>Delivery condition:</u> Standard material law <u>Relubricated:</u> Standard material law</p>	<p>CASE 4: <u>Delivery condition:</u> Standard material law <u>Relubricated:</u> Improvement potential with inhomogeneous material description</p>

Therefore, a new inhomogeneous material law was created, which offers an improved description of CJPEs that are strongly affected by the die-cutting of its components.

Table 4.2 summarizes the need of different material descriptions, in agreement with the classification made in *Chapter 3*: according to the difference in material strength between male and female components.

An inhomogeneous material description is advisable in the following cases:

- When materials with similar strengths are joined, and the production process of the components may have been altered the relative strength between them.

- If the components have been die-cut from a soft bulk material, whose strength will strongly vary after die-cutting.
- When the energy ratio used to deform the components is high in relation to the energy dissipated as friction (for example in lubricated components).

Thereby, this chapter revealed the methods to describe the material behavior of any kind of CJP. All the results shown in this chapter are however simulated with fitted friction coefficients. This is an established procedure, since the correct description of the whole F_1 - x_1 progression and the validation in different geometries of the same friction coefficient should ensure the correctness of this assumption.

Nevertheless, the friction coefficients will be measured in the following chapter and the interactions between the material and frictional descriptions will be assessed.

Chapter 5

Friction characterization

The coefficient of friction determines the strength of many types of mechanical joints [Nol74, Sta11, Xie00].

The coefficient of friction directly correlates with the strength of a CJC, since retention forces are basically frictional. Thus, the understanding of the friction mechanisms during the CJP, is essential for the correct design of CJC and the simulation of the insertion process.

In press-fit connectors, both the insertion and the retention forces are basically frictional. Many methods and experimental setups have been presented in order to determine friction coefficients for these connectors [Boi10, Cor03, Man07, Toh06].

The insertion forces of massive CJC are a combination of friction forces and the forces needed for the plastic deformation of the components.

Therefore, in this chapter the suitability of the established friction laws for the simulation of massive CJPs is analyzed, friction coefficients are measured, and the interaction between friction and material laws are discussed.

5.1 State of the art

5.1.1 Friction between metallic surfaces

Bowden and Tabor suggested [Bow43, Bow45] that the frictional force may generally be written as:

$$F_f = S + P \quad (5.1)$$

being S the force required to shear the metallic junctions and P the force required to displace the softer metal from the path of the slider.

The ploughing term P is usually neglected. However, for friction between surfaces with similar hardness is especially difficult to evaluate separately S and P .

If the ploughing term is neglected

$$F_f = S = A_r \cdot s \quad (5.2)$$

being A_r the real contact area and s the shear strength of the material. With any particular junction or point of contact between the metals, one of the two following conditions may occur:

- i. The strength of the adhesion between the metals is higher than the shear strength of the softest metal. If the fraction of the total area of contact over which this occurs is α , the frictional resistance due to the adherence will be $s_1 \cdot \alpha \cdot A_p$, where s_1 is the shear strength of the softest material.
- ii. The shear strength of the softest metal is greater than the strength of the junction between the metals. The strength of the junction, s_2 , is not necessarily constant.

Thus, the total shearing force, S , will be:

$$S = A_r \cdot (s_1 \cdot a + (1-a) s_2) \quad (5.3)$$

Kragelskii [Kra65] classified the types of destruction of the frictional bonds more generally as represented in Figure 5.1.

This classification can be correlated to the different *cases* of CJPEs presented in *Chapter 3*.

Case 1A and *case 4* are a combination of the type I and II destruction of bonds pictured in Figure 5.1. *Case 3* CJPEs are also a combination of these two types of mechanisms, with a predominant type II plastic displacement of the softest material.

The adhesive wear in *case 1B* can be attributed to the type V destruction of frictional bonds. The chip formation in *case 2* is equivalent to the cutting of the material represented as type III. These two types of CJPEs (*case 2* and *case 1B*) have already been presented as unsuitable for a robust insertion process.

Moreover, type IV destruction of surface films occurs in every insertion process with the thin oxide layers present in the copper components.

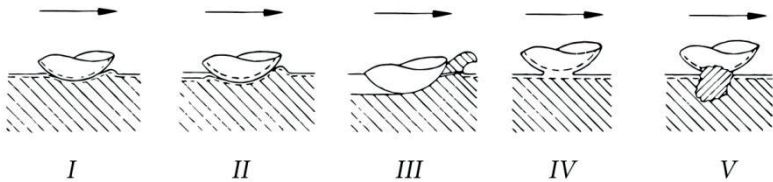


Figure 5.1: The main types of destruction of frictional bonds. I) elastic displacement, II) plastic displacement, III) cutting of the material, IV) destruction of surface films, V) destruction of bulk material [Kra65].

5.1.2 Friction in the finite element method

The early work of Coulomb and Amontons led to the following laws [Bow43]:

- i. The frictional force is independent of the area of the contacting bodies
- ii. The frictional force is proportional to the applied load

The first law holds because the real area of contact is very small and almost independent of the apparent area, since the contact only occurs locally in the surface irregularities. The second law can be explained in the case of plastic contact, due to the proportionality between the real contact area and the applied load.

The contact formulation in the FE simulation does not include the description of surface asperities and the real contact area. Tangential forces in a contact defined for a FE simulation are generally calculated according to Coulomb with a single factor: the friction coefficient.

$$\tau = \mu \cdot \sigma_n \quad (5.4)$$

This approach is the most widely used in FE simulations for the description of frictional contacts, and delivers good results for the simulation of cold-joining processes, where the assembly parts are elastic enough to absorb the overlay between them without high plastic strains [Kan85, Nol94].

The theory of plasticity differentiates the hydrostatic pressure for the calculation of the flow pressure. Assumed that the material is isotropic and homogeneous, the hydrostatic pressure has no influence on the material's flow [Par03].

Nonetheless, the hydrostatic pressure contributes to the normal pressure in a contact surface defined in a FE simulation. In the simulation of massive deformations very high hydrostatic pressures take place, and the use of the Coulomb friction model may lead to unrealistic high shear forces in the contact area that exceed the shear limit of the material [Eck 03, Neu03, Sch98].

Therefore, the approach of the shear model is used in simulations where high hydrostatic pressures occur in a contact surface. The shear model represents the shear stress in the contact zone, τ , in dependence on the shear limit of the softest contact material:

$$\tau = m \cdot k \quad (5.5)$$

k is the shear limit of the material and m is the shear model factor. Different k values are suggested in the literature for sheet forming simulations under diverse temperatures [Eck 03, Neu03].

The effect of high hydrostatic pressures does not apply for this model, and that is why it is widely used for the FE simulation of forming processes.

Unlike Coulomb's law, the shear model is able to account for the micro-scale wear in the contact surface, and is consistent with Tabor's theory (equation 5.3) when $(1-a) \cdot s_2 = 0$.

Nevertheless, copper parts tend to show strong adhesion during the insertion. In this case, the factor s_2 would become relevant, making the shear model unsuitable for the description of the joining process.

The limits of these existing contact definitions and the need of a new approach for the description of frictional situations are discussed in the following section.

5.2 Limitations of existing knowledge

The limitations of the two established friction laws for the FE simulation of metal forming and insertion processes are discussed in this section.

Configuration A samples are chosen for this purpose, since they exhibit different kinds of wear mechanisms, due to their high stiffness.

Figure 5.2 makes evident the need of a hybrid friction formulation if the maximal shear strength of the softest material is exceeded.

The maximal flow stress of the softest material was calculated as $\sigma_s / \sqrt{3}$, according to Von Mises' flow theory, being σ_s the yield strength of the softest contact material.

The hybrid model has proved to be able to describe the joining behavior for different geometrical layouts (overlays) in the material combination represented in Figure 5.2. Coulomb's friction law overestimates the joining forces, since the maximal shear strength that the contact area can transfer is exceeded, which becomes more pronounced for bigger overlays (overlay 2).

Coulomb's friction law exhibits the same limitations for the material combination represented in Figure 5.3. Nevertheless, the hybrid model is not able to predict the course of the joining forces with the accuracy exhibited in Figure 5.2. This is due to the higher hardness difference between materials, which makes the ploughing term presented in equation 5.1 more relevant.

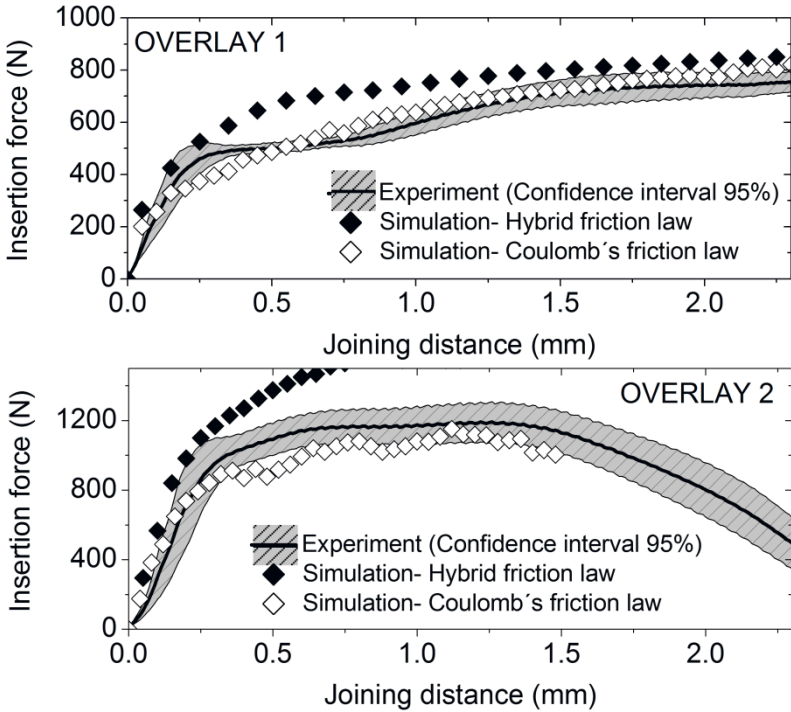


Figure 5.2: Coulombs friction vs. shear model in the simulation of a cold-joining process in *configuration A*. Material combination: Cu-ETP R250 bar and Cu-ETP R200 plate. Components were joined after relubrication.

Chapter 3 already presented both adhesive and abrasive wear as unsuitable for a robust CJP and a stable connector.

Therefore Coulomb's friction law should be able to represent all feasible insertion processes.

The maximal shear stress of the softest material calculated as $\sigma_s / \sqrt{3}$ will be therefore used as maximal admissible shear stress for the design of geometrical periphery and overlay, to avoid the loss of retention forces due to abrasive wear. This limit can be observed in the FE simulation, during the design of the CJC.

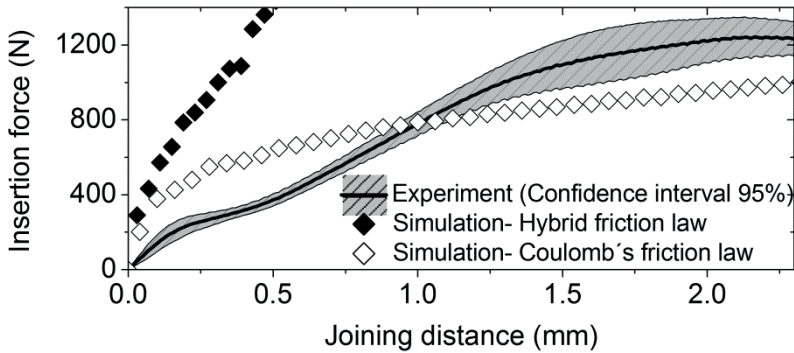


Figure 5.3: Coulombs friction vs. shear model in the simulation of a cold-joining process in *configuration A*. Material combination: Cu-ETP R250 bar and Cu-ETP R290 plate. Components were joined after relubrication.

Nevertheless, the onset of adhesive wear depends on many other factors, such as lubrication, the strength difference between both contact materials, and the geometrical stiffness of the connector.

Figure 5.4 presents the same material combination joined in Figure 5.2. Due to the lack of lubrication, the samples display a

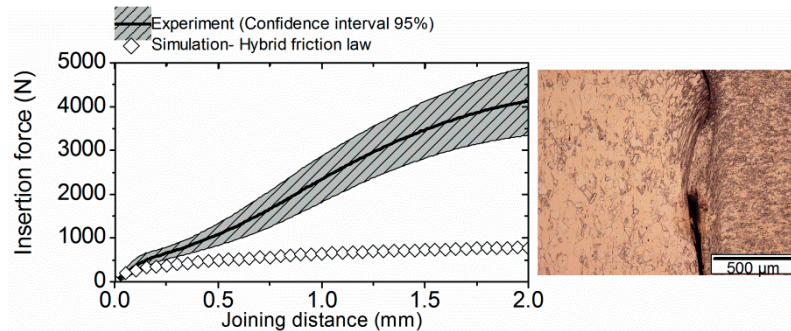


Figure 5.4 Coulombs friction vs. shear model in the simulation of a cold-joining process in *configuration A*. Material combination: Cu-ETP R250 bar and Cu-ETP R200 plate. Components were joined in delivery condition and adhesive wear was observed during the CJP.

strong adhesive wear. Coulomb's friction law presents convergence issues for the high occurring deformations. The hybrid law is not able to reproduce the phenomenon, since it is designed to describe the opposite term presented in equation 5.3.

From these results arise the main challenges to be solved in this chapter:

- i. The determination of validated friction coefficients for the FE simulation of CJPes.
- ii. The understanding of the onset of adhesive wear.

5.3 Friction test bench

A new test bench was built for the determination of friction coefficients and the study of adhesive wear phenomena in a similar set up to the conditions in the corresponding CJPes.

5.3.1 Experimental details


Samples

Samples were produced in order to replicate the surfaces in the punched edges of the *configuration B* CJCes.

Chapter 4 already determined that the surfaces at the punched edges of Cu-ETP R200 and Cu-ETP R250 materials are identical, due to the strain hardening during die-cutting. That is why, these samples did not show any significant difference on the friction test bench.

The material combinations that will be studied in the test bench are thus marked in grey in Table 5.1. Identical soft copper materials will be tested with each other, as well as identical harder

Table 5.1: Overview of the studied material combinations in the friction test bench.

		Fixed component		
		Cu-ETP R200	Cu-ETP R250	CuSn ₆ R500
				
Moving component	Cu-ETP R200		/	Chip formation
	Cu-ETP R250	/	/	
	CuSn ₆ R500		/	

bronze alloys. Moreover, the combination of the different materials will be tested, to assess the behavior of the wear mechanisms between samples with a high hardness difference.

All material combinations will be studied in delivery conditions, as well as after relubrication.

Construction

The friction test bench is incorporated in the Zwick Z010 static material testing machine.

The testing machine is used to apply the relative movement between components and to measure the frictional force.

The normal force applied during the friction measurements is measured online with an external force gauge.

The construction ensures that a perpendicular force to the contact area is applied during the process.

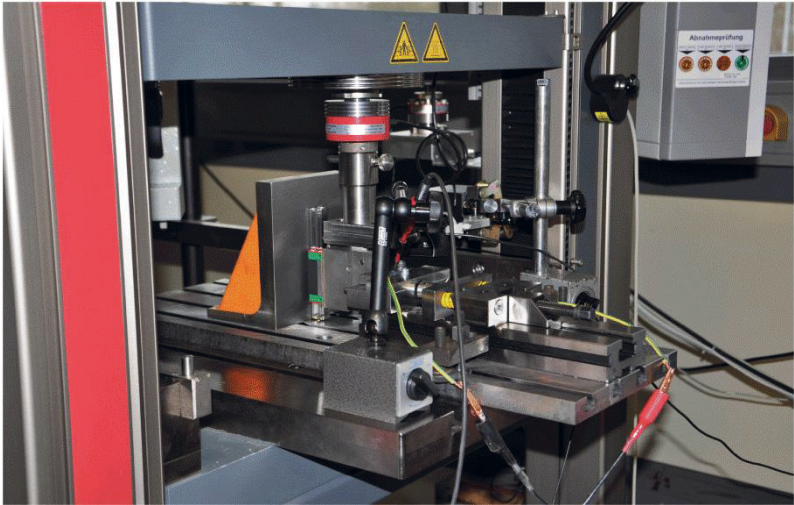


Figure 5.5: Overview of the new friction test bench.

Figure 5.5 displays the construction of the friction test bench in the material testing machine.

The operating method of the test bench is exemplified in Figure 5.6, as well as the fixture of the samples in the setting.

For every experiment a normal force is adjusted by means of a spring system.

Both the normal and frictional force, and the displacements are monitored during the experiment.

The absolute values of the friction forces and their progressions provide information about the friction coefficient between the surfaces and the wear mechanisms that may arise.

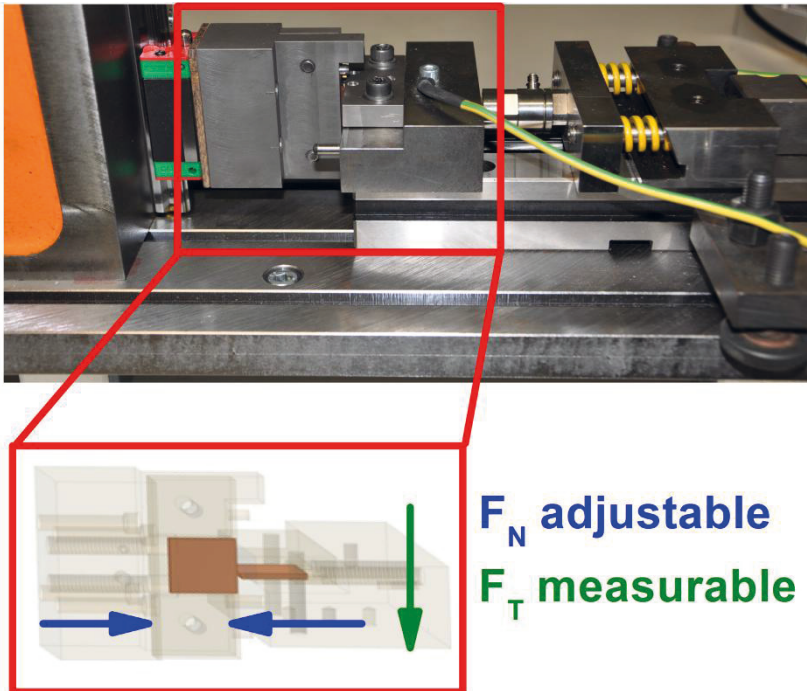


Figure 5.6: Detailed view of the measuring system and the situation of the samples in the new friction test bench.

5.3.2 Validation

The friction test bench is validated in lubricated steel, since this material does not show wear phenomena in the force spectrum studied for copper materials.

The friction between the components of the construction is pictured in Figure 5.7. Since the empty weight of the set-up is tared before the experiments, this frictional force is equal in both directions. This value is subtracted from all the results in this chapter.

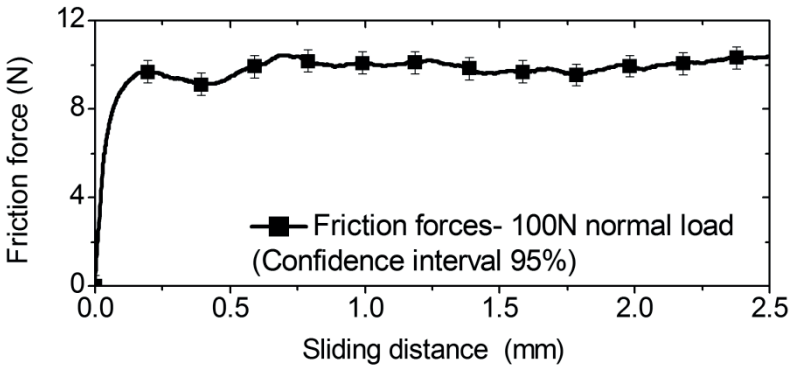


Figure 5.7: Construction's friction measured without any normal load.

The experiments in lubricated steel showed a constant friction force along the sliding distance, as it was expected for this frictional state (Figure 5.8).

Moreover, the friction coefficients calculated with the average frictional force measured in analogue curves to Figure 5.8, showed not to be dependent on the normal force used in the experiment (Figure 5.9).

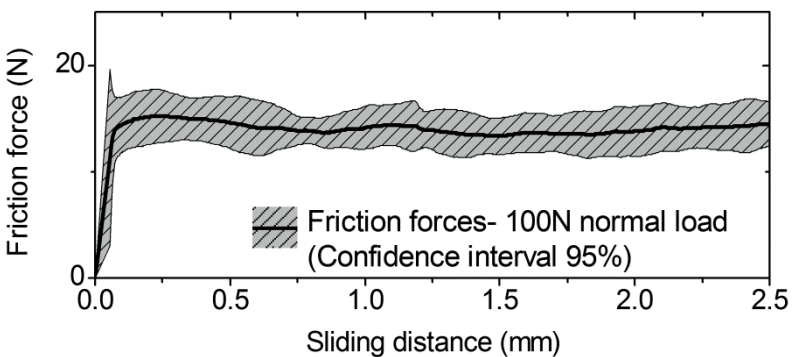


Figure 5.8: Validation of the test bench on lubricated steel. Sample friction curve.

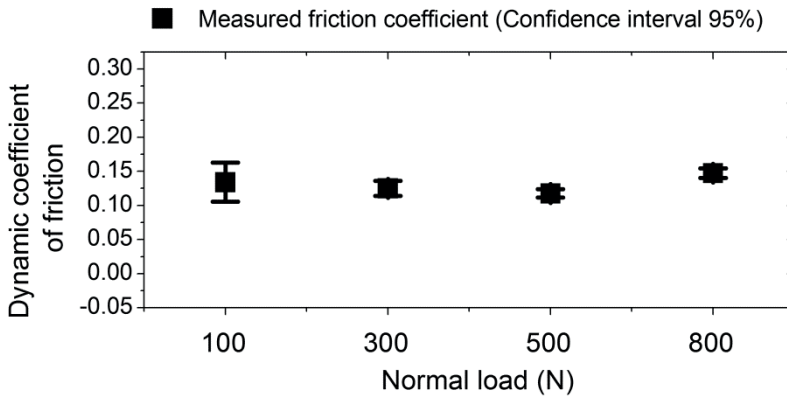


Figure 5.9: Validation of the test bench on lubricated steel. Friction coefficients for different normal loads.

Therefore, the test bench is considered suitable to measure friction coefficients, in cases where the frictional state is consistent with Coulomb's law.

5.3.3 Results

Friction coefficients

This section presents the friction coefficients measured for the different material combinations.

The frictional force progression in copper materials is exemplified in Figure 5.10. The worst case for the stability and reproducibility of these force-displacement devolutions occurs for the softest materials, due to the material deformation during the process, which leads to the broad confidence intervals for the friction coefficients shown in Figure 5.11 and Figure 5.12.

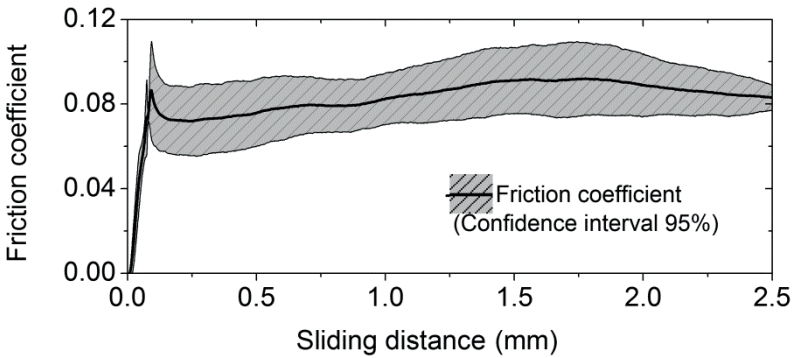


Figure 5.10: Sample friction coefficient curve between CU-ETP R200 samples.

The measured friction coefficients are compared in the following graphs to the friction coefficients used to fit the simulations of the CJPes, both in delivery condition and after relubrication.

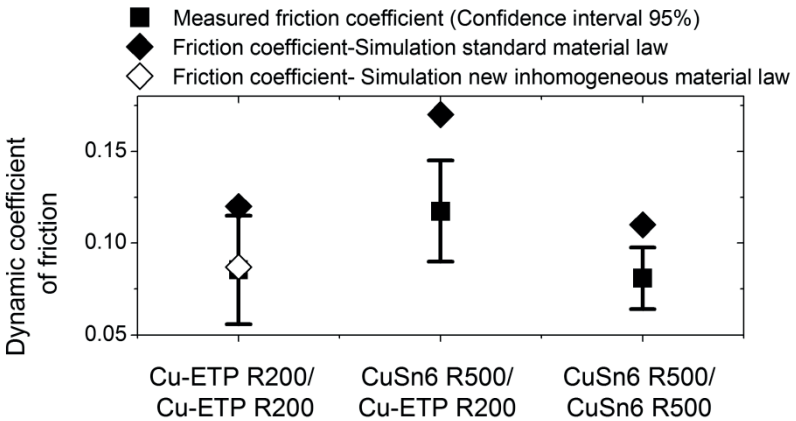


Figure 5.11: Friction coefficient between studied material combinations in delivery condition. Comparison between friction coefficients needed in the simulation and the measured values.

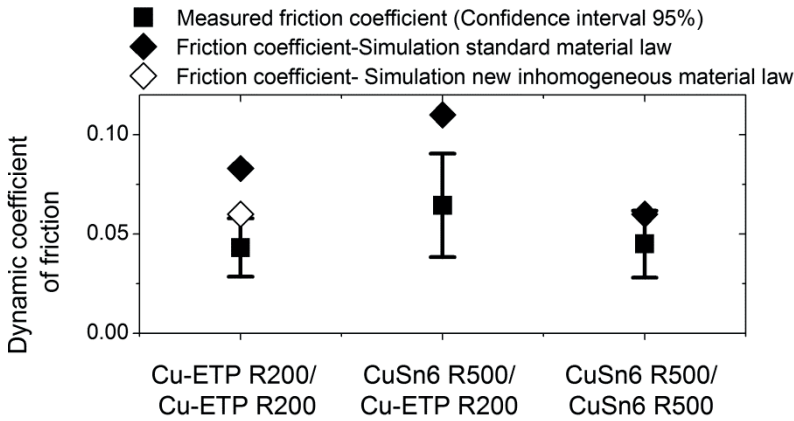


Figure 5.12: Friction coefficient between studied material combinations in relubricated condition. Comparison between friction coefficients needed in the simulation and the measured values.

The results presented in Figure 5.11 and Figure 5.12, reaffirm the necessity of the experimental validation of the friction coefficients used in the FE simulation of CJPs.

The reason for the disparity between measured and fitted values is also noticeable in these graphs.

The friction coefficients are specially overestimated in simulations where punched-edges in soft bulk materials are involved. This effect is compensated by a higher friction coefficient. These results reinforce again the validity of the inhomogeneous material law for copper materials developed in *Chapter 4*, which delivers far better results.

In conclusion, the interactions between material and friction law are not to be neglected. Fitting a friction coefficient may compensate other modeling errors in the simulation.

Moreover, a correct friction coefficient is needed for any reliability estimation of the connector.

Adhesive wear

The onset of adhesive wear in massive CJPes is strongly influenced by a variety of factors: poor lubrication, the high geometrical stiffness of the connector, and a disadvantageous choice of material combination.

Different wear mechanisms can also be detected in the friction test bench as represented in Figure 5.13. Not only the material transfer between components is appreciable under the microscope, but the force- displacement curves show also a noticeable increase in friction forces, if adhesive wear takes place. In the case of severe adhesive wear, components are joint after the experiment.

Chip formation (major abrasive wear) is also detectable by a characteristic F-x progression.

Coulomb's friction is characterized, as presented in the previous section, by a constant friction force.

The purpose of this section is quantifying the tendency to adhesive wear for different material combinations and lubrication states. Nevertheless, the contact area between samples during the experiments in the test bench, is not loaded under an homogeneous load.

That is why, a FE simulation is necessary to assure the transferability of the values detected in the test bench to the material loading during the CJPes. Figure 5.14 shows an example of a non homogeneous contact area during the experiments. The maximal normal stress (included hydrostatic pressure) transmitted

between the contact elements in these FE simulations (σ_{CN}) will be used as criteria to quantify the onset of adhesive wear.

The normal load applied to every studied variant will be increased up to the detection of adhesive wear mechanisms. The increase of the normal load is carried out in 100 N steps, due to the low reproducibility of the experiments, caused by the unstable nature of adhesive wear. Ten experimental repetitions will be carried out for every load level.

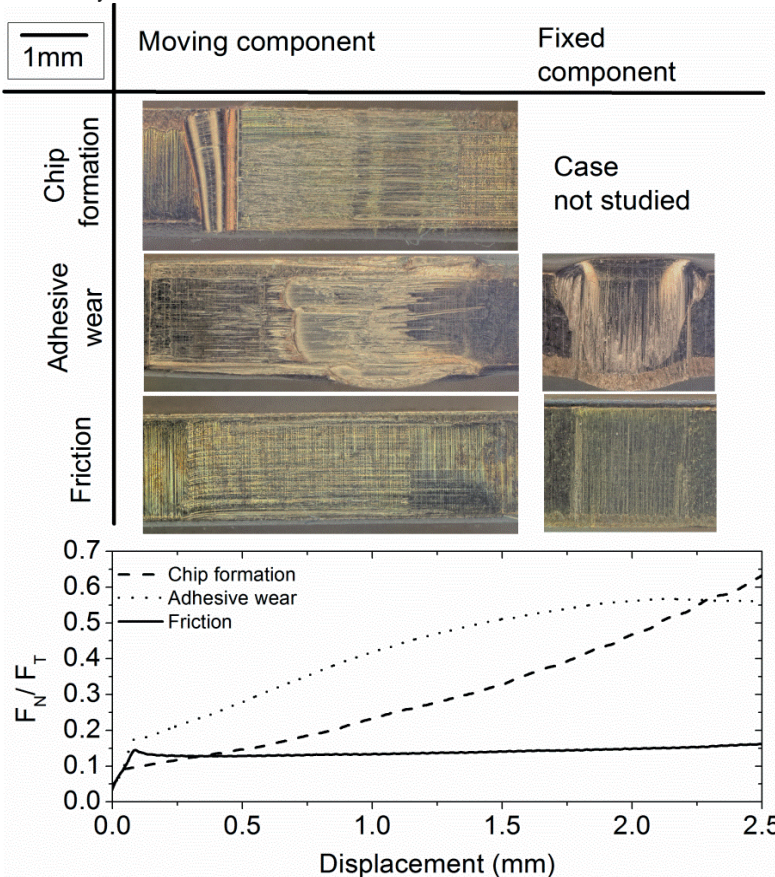


Figure 5.13: Different frictional situations detected in the friction test bench.

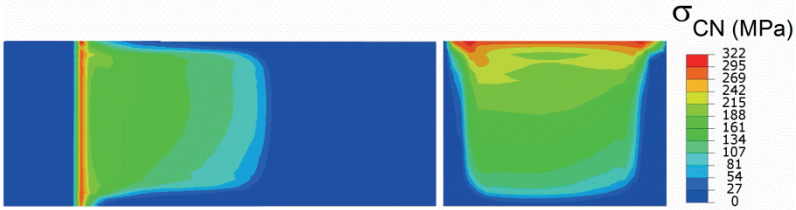


Figure 5.14: FE simulation of the experiments in the friction test bench. Calculation of maximal normal stresses acting in the contact area from the applied normal loads.

Figure 5.15 illustrates the different behavior of the diverse material combinations studied in delivery condition.

Contact materials with a low and similar mechanical strengths, tend, as expected [Pop11] to present adhesive wear.

Both Cu-ETP R200 samples in delivery condition started showing constant adhesive behavior with a normal load equivalent to a $\sigma_{CN} \approx 2200$ MPa in the FE simulation. However, some of the experimental repetitions (3 out of 10) with a $\sigma_{CN} \approx 830$ MPa already revealed adhesive wear. This evidences again the low reproducibility of this kind of experiments and confirms the lack of robustness of joining processes designed in the borderline to this wear phenomenon.

The material combination with a high hardness difference between contact partners (Cu-ETP R200 vs. CuSn₆ R500) did not display adhesive wear evidence in the whole realistic load spectrum for a CJC, despite the high plastic deformation of the softest material.

The same result was observed for the material combination between both CuSn₆ R500 samples.

Thus, only the material combination Cu-ETP R200 vs. Cu-ETP R200 is expected to be prone to adhesion in delivery condition, which can only be avoided by a relubrication of the samples or the observance of a low loading of the material during joining.

In fact, only material combinations between Cu-ETP R200 in/ or Cu-ETP R250 samples, showed adhesive wear during the CJPes (which display same surface characteristics at the punched edges).

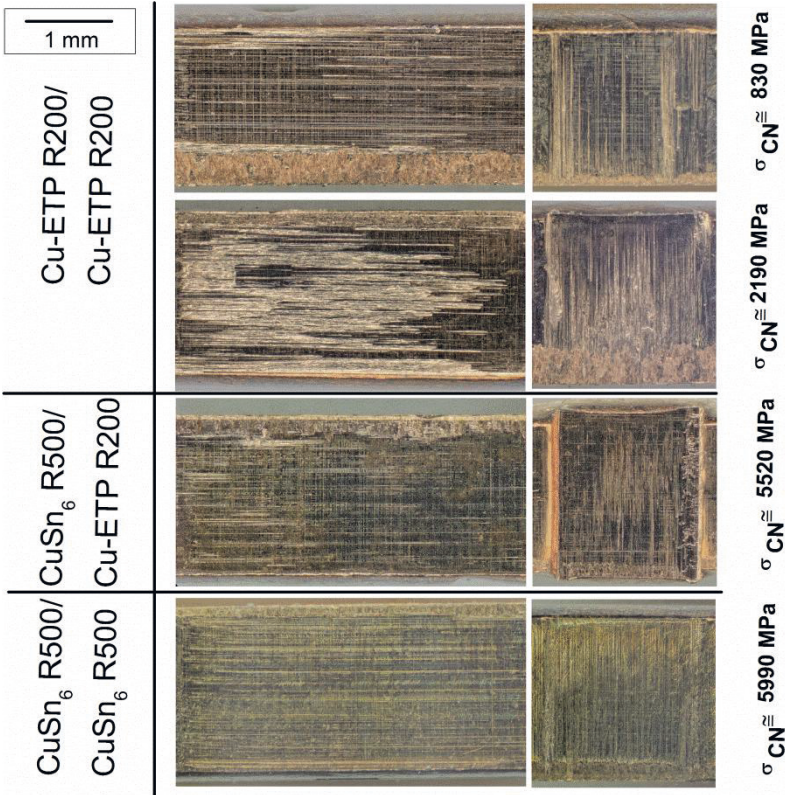


Figure 5.15: Sample surfaces for different material combinations after the experiments in the friction test bench in delivery condition of the parts. Left: moving parts. Right: fixed components.

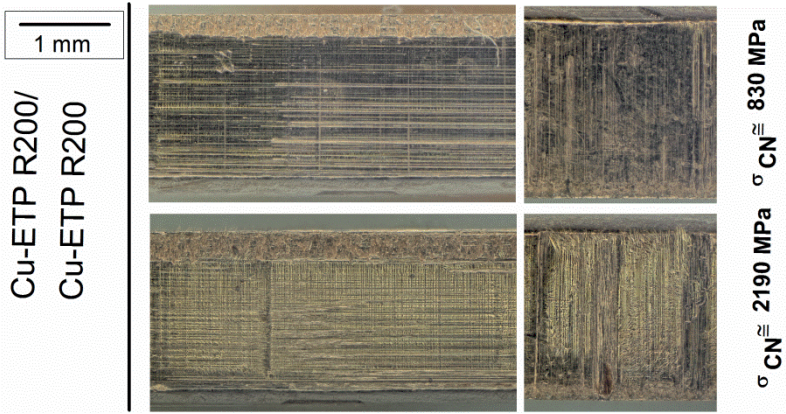


Figure 5.16: Sample surfaces after the experiments in the friction test bench for the material combination prone to adhesive wear (Cu-ETP R200/ Cu-ETP R200) after relubrication of the components. Left: moving parts. Right: fixed components.


Therefore, the results for the Cu-ETP R200 vs. Cu-ETP R200 samples are presented in Figure 5.16 for relubricated samples. The relubrication of the samples prevented the adhesion in 100% of the repeated experiments for the same critical loads detected in Figure 5.15.

These results are in agreement with the critical loads corresponding to the studied CJPEs. Table 5.2 shows the joining processes of the material combinations, which are susceptible to adhesion. The variants that delivered a non robust CJP due to adhesive wear are marked in grey. The values of the simulated σ_{CN} confirm that the critical stress level for the normal load transmitted in the contact elements starts at about 800 MPa.

On the other hand, no adhesion was detected in the joining processes of the same contact variants with relubricated samples.

Nevertheless, the transferability of the results from the frictional test bench to the real CJPEs is dependent of many external

Table 5.2: Joining behavior of the CJPes prone to adhesive wear in delivery condition. The unstable processes with adhesive wear are marked in grey. Numbers represent the σ_{CN} in MPa.

		 Material of female component	
		Cu-ETP R200	Cu-ETP R250
Material of male component	Cu-ETP R200	OVERLAY 1: 430 OVERLAY 2: 500	OVERLAY 1: 608 OVERLAY 2: 712
	Cu-ETP R250	OVERLAY 1: 490 OVERLAY 2: 550	OVERLAY 1: 820 OVERLAY 2: 910

factors, such as small geometrical imperfections and changes in surface quality.

In conclusion, the joining of equally hard copper components is discouraged, due to the susceptibility to adhesive behavior, and the hardly predictable behavior of this phenomenon. A thorough lubrication of the samples has to be assured if such a CJP is pursued.

No impediment is to be foreseen for the joining of hard materials or material combination with a high hardness difference in this respect.

5.4 Summary

The objectives of this chapter were experimentally determining the friction coefficients between components, and delivering guidelines for the control of the wear mechanisms.

A new experimental setup was used to get to the following conclusions:

5.4.1 Friction coefficient

The results in this chapter reveal the strong interaction between the material characterization and the friction law. An inaccurate material law may be compensated by a non realistic friction coefficient, if friction is used to fit the insertion curves. This finding validated again the improved accuracy of the material model, if the inhomogeneous material description at punched edges is applied.

Measurements of friction coefficients directly on punched edges determined that 0.08 and 0.05 are good estimations for friction coefficients in surfaces in delivery condition and relubricated surfaces respectively.

Fitted friction coefficients can be used for geometry and lay out optimizations, but validated values are necessary for reliability studies.

5.4.2 Wear tendency

Both abrasive and adhesive wear are to be avoided in a CJP. Abrasive wear counts against the retention force of the

connector. Adhesive wear on the other hand, leads to increased insertion forces and a highly unstable insertion process.

Abrasive wear

Abrasive wear occurs if two contact partners with very disparate strengths are joined. In section 3.1, *case 2* was already presented as not joinable, due to chip formation.

For *case 3* CJPs the critical strength for abrasive wear has to be considered, in order not to lose retention force.

Adhesive wear

The tendency to adhesive wear is also determined by the material combination. Similar materials tend to form microweldings.

Despite the high scattering of the results and the unpredictable nature of wear mechanisms, critical loads were defined for different material combinations. An FE simulation can support the optimization of layouts to avoid stress peaks, and thus, the incidence of wear.

Only soft copper components proved to be susceptible to adhesive wear if joint with each other in the studied range of loads and overlays.

The preferred material combinations for CJs presented in *Chapter 6* are based on these considerations to avoid wear.

Chapter 6

Implementation on the optimization of a real high power connector

This chapter centralizes the knowledge gained in previous chapters into the procedures for the design of a novel HPC and the FE modeling for CJPes.

This method is applied to the design of a real HPC.

6.1 Procedure for the optimization of a HPC

A schematic representation of the design cycle for a new HPC is shown in Table 6.1.

The first step towards a new design for a HPC is the selection of the material for both components. The favorite material combinations can be deduced from the adhesive wear behavior studied in *Chapter 5* and the characteristic joining processes presented in *Chapter 3*.

Table 6.1: Procedure for the optimization of a HPC.

1. MATERIAL COMBINATION CHOICE	Criteria: Maximize contact force and avoid adhesive wear tendency
Order of preferred combinations (see section 3.1.2 and Chapter 5): <ul style="list-style-type: none"> • Case 4 • Case 3 • Case 1A 	
2. GEOMETRY OPTIMIZATION/ PERIPHERY-<i>Simulation-Aided</i>	Criteria: Symmetric contact area. Avoid localized stress peaks
3. OVERLAY OPTIMIZATION- <i>Simulation-Aided</i>	
	<i>Criteria</i>
<i>Case 4</i>	Observe shear limit
<i>Case 3</i>	Find the optimum F_{out} / F_{in}
<i>Case 1A</i>	Observe adhesive wear tendency

The right material selection must assure the absence of wear phenomena for a broad spectrum of loads. Moreover, the material combination must be chosen in order to maximize the joining forces at the end of the joining process, since these forces directly correlate to the reliability of the connector.

The design of the connector's periphery must assure that the material is homogeneously loaded in the contact area. That way, stress peaks that may lead to wear between surfaces can be avoided and a high retention forces are achieved.

The selection of the right overlay between components is also a crucial part of the design process. This selection must provide a strong connector without overloading the material.

The FE simulation can powerfully support the design of the periphery and the overlay. Simulated stress states in the contact area can be observed for the design of the outer geometry. A simulation of the optimum geometry with different overlays, allows for the selection of the maximal retention force under the observation of the load limits presented in *Chapter 5*.

This design cycle is demonstrated with a real example in section 6.2.

The steps to be followed to build a FE model for the force-fitting simulation are represented in Table 6.2.

The general settings of the model have been briefly stated in *Chapter 3*.

Chapter 4 and *Chapter 5* proved the need of an inhomogeneous material law at punched edges for a correct description of the joining process with a real friction coefficient. Nevertheless, if the relative hardness between the components isn't altered by the stamping process, the bulk material data correctly represents the building of the contact area during the CJP. Thus, standard material data would be sufficient for geometrical comparisons.

Regarding the friction formulation, guidelines for avoiding wear phenomena were given in *Chapter 5*, since wear mechanisms lead to a deficient reliability and a non robust joining process. Therefore reference friction coefficients for Coulomb's friction formulation are recommended.

Table 6.2: Procedure for the FE simulation of a CJP.

1. GENERAL SETTINGS (see <i>Chapter 3</i>)	
<ul style="list-style-type: none"> • Solver: Implicit solver. Consider explicit solver in case of large 3D models. • Contact: Penalty. • Mesh: Reference values for mesh size analysis (element size in the contact area): <ul style="list-style-type: none"> – Rigid geometries with strong localized stresses: 30 μm – Compliant geometries: 80 μm 	
2. MATERIAL PROPERTIES (see <i>Chapter 4</i>)	
If goal= periphery optimization/layout comparison	Homogeneous material law: material data library/ tensile test
If goal= prediction joining/ retention forces	Local material characterization at punched edges
3. FRICTION LAW (see <i>Chapter 5</i>)	
If adhesive wear is detected	No robust process No simulation
If $\sigma_{\text{shear,max}} > \sigma_y / \sqrt{3}$	Hybrid law (avoid reaching the limit in the whole contact area)
else	Coulomb's friction Reference friction coefficients: <ul style="list-style-type: none"> • Delivery condition: 0.08 • Relubricated: 0.05

6.2 Optimization of a real HPC

The procedures presented in section 6.1. are applied in this section to the design of a real HPC.

6.2.1 Framework conditions

The design of this CJC will find application in the next generation of the inverter presented in Figure 1.1. The material combination, as well as the plate thickness and the designed space are boundary conditions from the design of the rest of the inverter.

The female component has to be produced from a Cu-ETP R250 copper sheet with a 0.8 mm thickness. The male component has to be produced from a 3 mm thick Cu-ETP R200 sheet.

The periphery and the overlay between components can be optimized.

6.2.2 Results

Material selection

The material combination given as framework would lead to a *case 2* joining behavior (see section 3.1.2), since the male component is made of a softer material than the female one.

To avoid this unstable joining behavior, the male component will be embossed and thus work-hardened to reach a higher strength than the female component.

Thus, a *case 3* joining behavior is expected.

Periphery optimization

The design of the connector's periphery for a homogeneous stress on the contact area is represented in Figure 6.1. The simulation shows a symmetric stress state at both sides of the contact area, provided by the cavities in the plate.

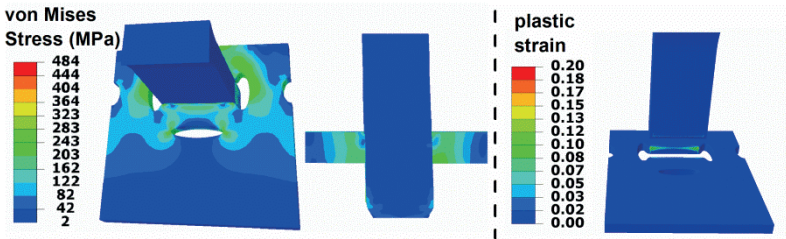


Figure 6.1: Design of the periphery of the optimized HPC. Left: stress-strain state of the HPC after the cold-joining process. Right: plastic strain on the components after pressing them out.

Moreover the perpendicular reliefs in the plate at both sides of the pin prevent stress peaks at the pin's edges and favor the homogeneous stress distribution in the plate.

The absence of unnecessary loading of the material is also appreciable in the low plastic strains on the components after force-fitting and pressing them out. Plastic deformation wouldn't contribute to the reliability of the connector, since the elastic component of the deformation holds the connector together.

Overlay optimization

Figure 6.2 analyzes the force-fitting and retention loads for different overlays. The insertion force (F_i) against the overlay is a monotonically increasing function, the extraction force (F_o) on the contrary is not.

The extraction force reaches a maximum for a certain overlay, from which the plastic deformation of the components prevents the retention forces to increase. This behavior can be explained recalling the knowledge gained in section 3.1.2.: the *case 3* F_1 - X_1 progression would have a greater maximal F_1 for a higher overlay but would converge to a same retention force at the end of the curve.

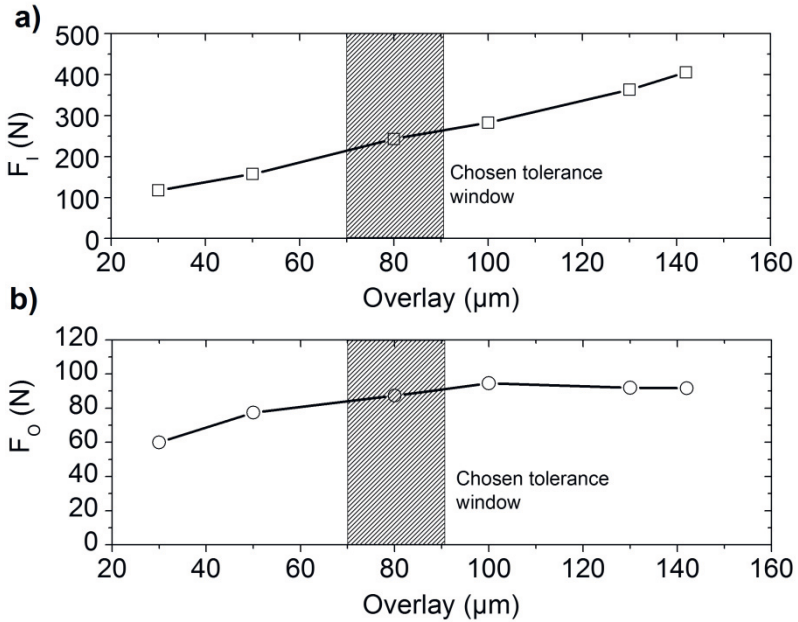


Figure 6.2: Simulative analysis of the optimal overlay. Each point in the graph represents a simulation with a different overlay. a) Force-fitting load against different overlays. b) Pressing-out load against different overlays.

The criteria applied for the selection of the tolerance window for the overlay, are achieving the maximal F_O keeping the F_I as low as possible, to avoid overloading the material.

Die-cutting produces very low scattering of the dimensions but the nominal dimension can vary from the desired one. That is why, the tolerance window represented in Figure 6.2 was chosen for values slightly under the maximum extraction force point, in order to assure that no excessive overlays may be produced.

6.3 New optimized connector

The simulatively optimized components presented in Figure 6.3 have been produced and analyzed for the revalidation of the simulation model.

6.3.1 Samples

Figure 6.4 shows the real components and HPC optimized by means of the developed methodology.

The pin was embossed up to the desired thickness for the contact area. Therefore the material went through a strong work hardening and material data corresponding to Cu-ETP R360 was assumed for the contact area.

The plates for the validation samples were eroded and the contact area was embossed afterwards. Therefore, the edges at the contact area have to be reanalyzed to assess the hardness distribution after such a production process.

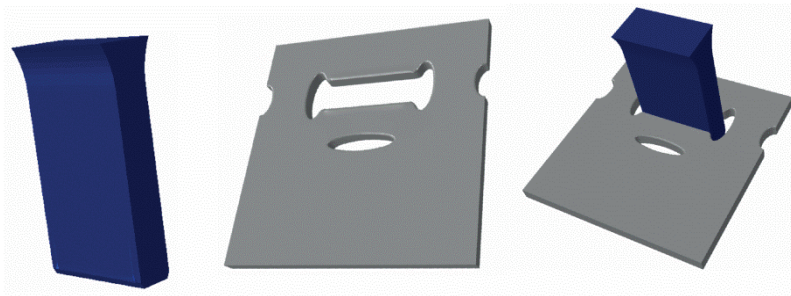


Figure 6.3: Optimized components for a real HPC.

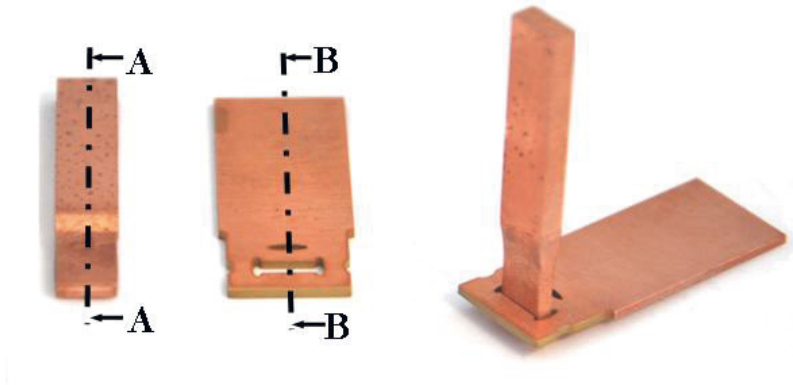


Figure 6.4: HPC designed according to the new simulation method.

Figure 6.5 shows the cross-sections of both contact partners, and schematically represents the position of the hardness screenings that are shown in Figure 6.6, Figure 6.7, and Figure 6.8.

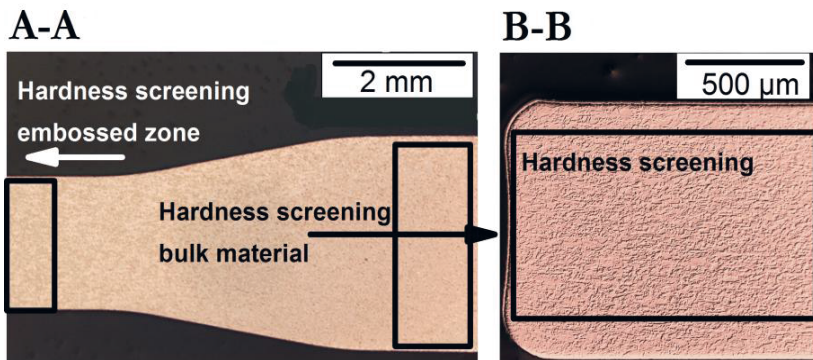


Figure 6.5: Cross-section of the components and representation of the hardness screenings' situation. Left: pin. Right: plate.

The hardness measurements on the embossed area of the pin (Figure 6.6) show hardness values around 140 HV. The correlation between flow curves and hardness presented in Figure 4.26 validates the assumption that the material properties of Cu-ETP R360 should be assumed in this area.

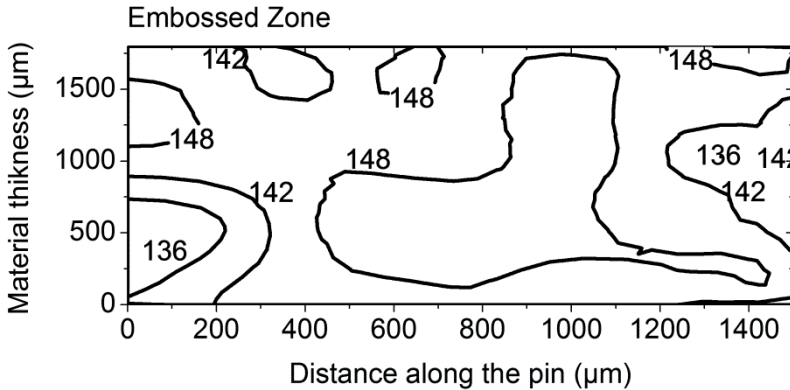


Figure 6.6: Hardness screening on the embossed area of the new HPC's pin. The measured area is marked on the left side of the left picture in Figure 6.5. The numbers represent the hardness values in HV (0.3/ 10/ 40/ 10).

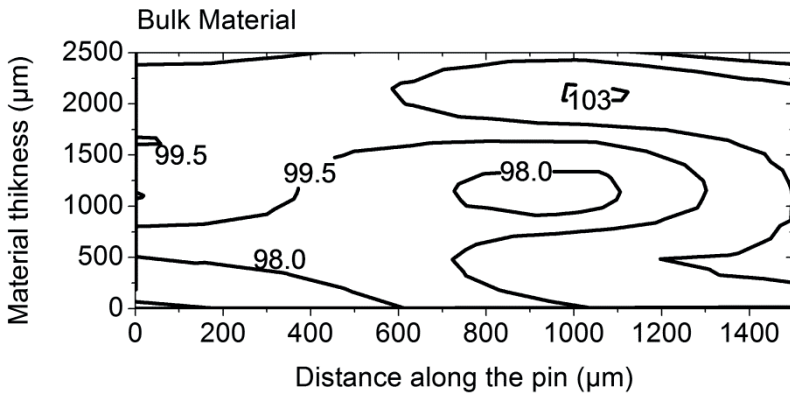


Figure 6.7: Hardness screening on the bulk material of the new HPC's pin. The measured area is marked on the right side of the left picture in Figure 6.5. The numbers represent the hardness values in HV (0.3/ 10/ 40/ 10).

The nanoindentation screening in the pin's bulk material is shown in Figure 6.7. Comparing these hardness values with the characteristic values represented in Figure 4.26, reveals that the 3 mm copper sheet used to make these components has a strength between a Cu-ETP R200 and a Cu-ETP R250 material. Nevertheless, a sensitivity analysis carried out on the simulation model, exhibits that the material model chosen for the bulk material of the pin does not affect the simulation results, since only the embossed zone is relevant in the contact area.

The material properties in the contact area of the plate are studied in Figure 6.8. Unlike the punched edges, the embossed contours do not reveal a measurable hardness gradient. Moreover, the hardness screening indicates that the flow curve determined for Cu-ETP R250 corresponds to the hardness values, and thus to the material behavior in this area.

Consequently, the material properties assumed for the simulative optimization of the connector, have been validated after studying the finished parts through nanoindentation measurements.

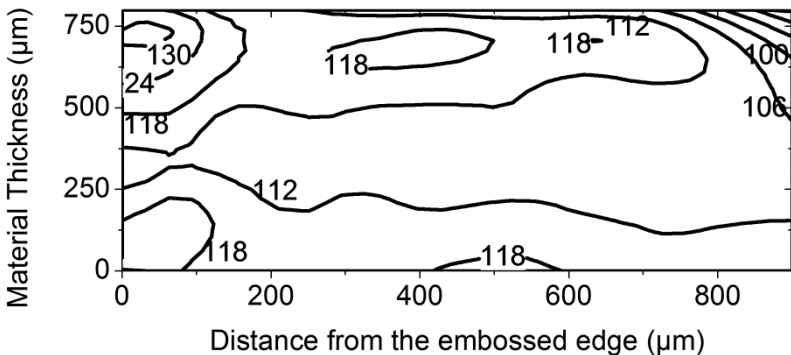


Figure 6.8: Hardness screening on contact area of the new HPC's plate. The measured area is marked on the right picture in Figure 6.5. The numbers represent the hardness values in HV (0.3/ 10/ 40/ 10).

6.3.2 Cold-joining Process

Figure 6.9 reveals the joining behavior predicted by the simulation model for the optimized HPC. This F-x progression is juxtaposed to the experimental force-fitting curves after the HPC's production.

Regarding friction, the CJC was designed to avoid micro-abrasive wear and the reference friction coefficient value determined in *Chapter 5* for components in delivery conditions was used.

The simulation model was refined after the study of the real parts (slight geometry change of the plate's contact area and measured overlay).

In Figure 6.9 comes into view that the simulation model predicted fairly well the joining behavior of the connector, both in terms of maximal insertion force and the retention forces at the end of the CJP.

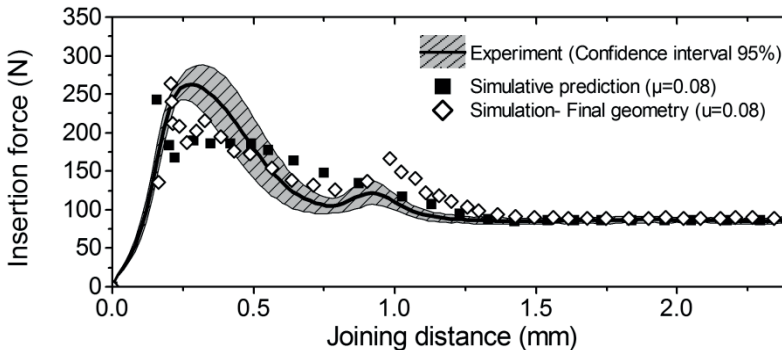


Figure 6.9: Comparison between simulated and experimental F-x progressions of the HPC. A constant friction coefficient obtained from the studies in *Chapter 5* was used for the simulation.

The overlay sensitivity study carried out in Figure 6.2 is also inspected in view of the real insertion and extraction forces measured in the experimental CJP.

As already displayed in Figure 6.9 the maximal insertion force is accurately described by the simulation model. The experimental extraction forces have a higher scattering, and the simulation model predicts strength of the connector into these confidence lines.

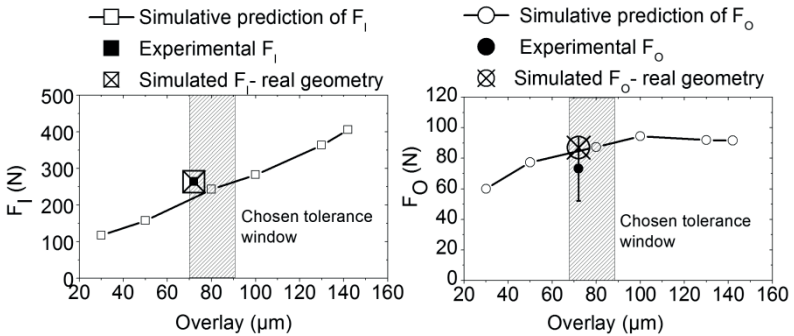


Figure 6.10: Comparison between the real and the predicted maximal insertion and extraction forces of the HPC.

Chapter 7

Summary & Outlook

This thesis presents the design and FE simulation of novel massive copper cold-joined connectors for high power applications.

A real HPC was designed following the guidelines developed in this work. The FE simulation proved to be able to represent the joining process (Figure 7.1) and throws new light on the optimization potential of the CJC.

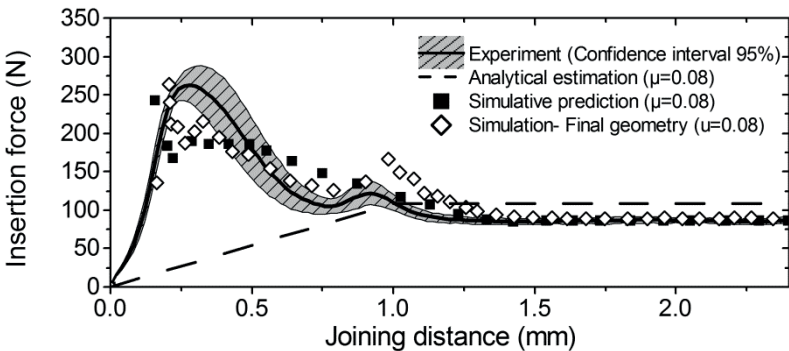


Figure 7.1: Prediction and Reproduction of a real CJP by means of the new FE simulation methodology and its comparison to the state of the art.

The model is not only able to reproduce the real joining process, but also improved the prediction of joining forces significantly, in comparison to analytical approaches presented in *Chapter 2*.

The setup of this capable simulation model is based on separately validated material and friction models.

The challenges for the material characterizations of massive copper components derive from the significant changes in material properties that they undergo during their production process. As defined in *Chapter 1*, an improved material characterization was reached, by means of a material characterization for high plastic strains, which accounts for the stress situation and the work hardening of the components during their production process.

The aims defined for this thesis regarding frictional characterization were achieved in a new test bench, which delivered validated friction coefficients for the FE simulation, and new insights about material combinations for a robust CJP without wear phenomena.

This methodology is applicable to the design of all kinds of copper cold-joined connectors and extendable to other materials, such as aluminum or steel. The extension of the methodology to new light-weight materials opens new fields of applications in the automotive industry, since cold-joining is gaining relevance in the frame-and-body construction.

This simulation model can be extended and used as the original state of the HPC for reliability simulations.

Publications

- [Ari12] E. Aristizabal, F. Günter, P. Schaaf, “New method to characterize material properties of copper by microindentation”, in: *Materials for Energy and Power Engineering*, Universitätsverlag Ilmenau, pp. 29-45, 2012.
- [Ari13] E. Aristizabal, F. Günter, P. Schaaf, “Challenges in design and simulation of cold-joined connectors for high current applications”, *Proceedings of 4th Symposium Connectors*, Lemgo, 2013.
- [Ari14a] E. Aristizabal, F. Günter, P. Schaaf, “Impact of inhomogeneous material description for punched edges on the force-fitting simulation of copper high current connectors”, *27th International Conference on Electrical Contacts*, Dresden, 2014.
- [Ari14b] E. Aristizabal, F. Günter, M. Hopfeld, P. Schaaf, “Improved description of the flow characteristics of copper for the finite element simulation of the cold-joining process of high current electrical contacts”, *Advanced Engineering Materials*, DOI:10.1002, 2014.

References

- [Abe03] M. Abendroth, M. Kuna, “Determination of deformation and failure properties of ductile materials by means of the small punch test and neural networks”, *Computational Materials Science*, vol. 28, pp. 633-644, 2003.
- [Ahn00] J. H. Ahn, “Effects of work-hardening characteristics on evaluating flow properties from indentation load-depth curve”, in: *Proceedings of Mikromat International Conference*, pp. 400-403, Berlin, 2000.
- [Ahn01] J. H. Ahn, D. Kwon, “Derivation of plastic stress-strain relationship from ball indentations: Examination of strain definition and pileup effect”, *Journal of Materials Science*, vol. 16, pp.3170-3178, 2001.
- [ASM92] American Society for Metals, *Friction, Lubrication and Wear Technology*. ASM Handbook vol. 18, 1992.
- [Ban05] D. Banabic, H. Aretz, D. S. Comsa, L. Paraianu, “An improved analytical description of orthotropy in metallic sheets”, *International Journal of Plasticity*, vol. 21, pp. 493-512, 2005.

- [Biw95] S. Biwa, B. Storakers, “An analysis of fully plastic Brinell indentation”, *Journal of the Mechanics and Physics of Solids*, vol. 43, pp. 1303-1333, 1995.
- [Böh03] T. Böhlke, A. Bertram, “Asymptotic values of elastic anisotropy in polycrystalline copper for uniaxial tension and compression”, *Computational Materials Science*, vol. 26, pp. 13-19, 2003.
- [Boi10] L. Boissonnet, B. Duffau, P. Montmitonnet, “Tribological study of a press-fit assembling process”, ICTMP Nice, 2010.
- [Bor08] W. Borchardt-Ott, *Kristallographie: eine Einführung für Naturwissenschaftler*, Springer, 2008.
- [Bow43] F. P. Bowden, A. J. M. Moore, D. Tabor, “The ploughing and adhesion of sliding metals”, *J. Appl. Phys.*, vol. 14, pp.90-91, 1943.
- [Bow45] F. P. Bowden, D. Tabor, “Friction and lubrication”, *Ann. Rep. Chem. Soc.*, vol. 42, pp. 20-46, 1945.
- [Bow53] F. P. Bowden, D. Tabor, *The Friction and Lubrication of Solids*. Oxford at the Clarendon Press, 1953.
- [Cho12] M. A. Chowdhury, D. M. Nuruzzaman, A. H. Mia, M. L. Rahaman, “Friction coefficient of different material pairs under different normal loads and sliding velocities”, *Tribology in Industry*, vol 34, pp. 18-23, 2012.
- [Cor03] N. Corman, M. Myers, C. Copper, “Friction behavior of press-fit applications: test apparatus and methodology”, *Proceedings of 49th Holm Conference on electrical Contacts*, September 2003.

- [Czi78] H. Czichos, Tribology: a systems approach to the science and technology of friction, lubrication and wear. Elsevier, 1978.
- [Dav01] J. R. Davis, Copper and Copper Alloys. ASM International, 2001.
- [Dav97] J. R. Davis, Concise Metals Engineering Data Book. ASM International, 1997.
- [Die94] H. Dietrich et al., Mechanische Werkstoffprüfung. Expert Verlag, 2nd edition, 1994.
- [DIN01] “Pressverbände- Berechnungsgrundlagen und Gestaltungsregeln”, Ref. Nr. DIN 7190:2001-02, Deutsches Institut für Normung e. V., 2001.
- [DIN03a] “Fertigungsverfahren Fügen- Teil 0: Allgemeines- Einordnung, Unterteilung, Begriffe”, Ref. Nr. DIN 8593-0:2003-09, Deutsches Institut für Normung e. V., 2003.
- [DIN03b] “Fertigungsverfahren Fügen- Teil 3: Anpressen, Einpressen- Einordnung, Unterteilung, Begriffe”, Ref. Nr. DIN 8593-3:2003-09, Deutsches Institut für Normung e. V., 2003.
- [DIN03c] “Fertigungsverfahren Fügen- Teil 5: Fügen durch Umformen- Einordnung, Unterteilung, Begriffe”, Ref. Nr. DIN 8593-5:2003-09, Deutsches Institut für Normung e. V., 2003.
- [DIN06] “Metallic materials - Vickers hardness test - Part 1: Test method”, Ref. Nr. DIN EN ISO 6507-1:2006-03, Deutsches Institut für Normung e. V., 2006.

- [DIN07] “Advanced technical ceramics - Mechanical properties of monolithic ceramics at room temperature - Part 2: Determination of Young's modulus, shear modulus and Poisson's ratio”, Ref. Nr. DIN EN 843-2:2007-03, Deutsches Institut für Normung e. V., 2007.
- [DIN09a] “Testing of metallic materials - Tensile test pieces”, Ref. Nr. DIN 50125:2009-07, Deutsches Institut für Normung e. V., 2009.
- [DIN09b] “Metallic materials - Tensile testing - Part 1: Method of test at room temperature”, Ref. Nr. DIN EN ISO 6892-1:2009-12, Deutsches Institut für Normung e. V., 2009.
- [DIN11] “Hochstrom Prüftechnik- Begriffe und Anforderungen für Hochstrom-Messungen”, Ref. Nr. DIN EN 62475/ VDE 0432-20, Deutsche Kommission Elektrotechnik Elektronik Informationstechnik im DIN und VDE, 2011.
- [DIN12] “Lötfreie Verbindungen- Teil 5: Einpressverbindungen- Allgemeine Anforderungen, Prüfverfahren und Anwendungshinweise”, Ref. Nr. DIN EN 60352-5:2012-10, Deutsche Kommission Elektrotechnik Elektronik Informationstechnik im DIN und VDE, 2012.
- [DIN12] “Metallic materials - Instrumented indentation test for hardness and materials parameters - Part 2: Verification and calibration of testing machines”, Ref. Nr. DIN EN ISO 14577-2:2012-03, Deutsches Institut für Normung e. V., 2012

- [DIN78] “Testing of Metallic Materials; Compression Test”, Ref. Nr. DIN 50106:1978-12, Deutsches Institut für Normung e. V., 1978.
- [DIN93] “Advanced technical ceramics; monolithic ceramics; general and textural properties; part 2: determination of density and porosity”, Ref. Nr. DIN EN 623-2:1993-11, Deutsches Institut für Normung e. V., 1993.
- [Dub94] Dubbel: Taschenbuch für den Maschinenbau. Ed. by W. Beitz and K. –H. Küttner, 18th edition, Springer Verlag, 1994.
- [DVS06] “Mechanisches Fügen- Konstruktion und Auslegung”, Ref. Nr. DVS/EFB 3470, DVS/EFB-Gemeinschaftsausschuss Mechanisches Fügen, 2006.
- [Eck09] J. Eckstein, Numerische und experimentelle Erweiterung der Verfahrensgrenzen beim Halbholzstanzen hochfester Bleche. IMWF/ MPA Universität Stuttgart, 2009.
- [Eng10] O. Engler, V. Randle, Texture analysis: Macrotecture, microtexture and orientation mapping. CRC Press, 2010.
- [Erd07] H. Erdogan, “Einfluss unterschiedlicher Geometrien und Werkstoffsysteme auf den Fügeprozess und die Eigenschaften von massiven Einpressverbindungen”. Utz, 2007.
- [Fuh03] E. Fuhrmann, Einführung in die Werkstoffkunde und Werkstoffprüfung. Expert Verlag, 2nd edition, 2003.

- [Ges03] H. Gese, S. Keller, V. Yeliseyev, H. Dell, "Ermittlung von Fließwiderstandskurven bei großen Formänderungen für die Blechumformsimulation", DVM-Tagung, Bad Nauheim, 2003.
- [Gün10] F. Günter, "Ausfallmechanismen, Ausfallmodelle und Zuverlässigkeitsbewertung von kalten Kontaktiertechniken", Universitätsverlag Ilmenau, 2010.
- [Hei09] T. Heinisch, Einpresstechnik: Entwicklung, Anwendung, Qualifizierung. Eugen Leuze Verlag, 2009.
- [Hill89] R. Hill, B. Storakers, A. B. Zzdunek, "A theoretical study of the Brinell hardness test", Proceedings of Real Society of London, vol. A423, pp.301-330, 1989.
- [Hus07] H. Erdogan, Einfluss unterschiedlicher Geometrien und Werkstoffsysteme auf den Fügeprozess und die Eigenschaften von massiven Einpressverbindungen. Herbert Utz Verlag, München, 2007.
- [Ign00] E. Ignatowitz, O. Spielvogel, F. D. Stricker, K. Tkotz, Werkstofftechnik für Elektroberufe. Verlag Europa Lehrmittel, 2000.
- [Kan85] T. Kanai, Y. Ando, S. Inagaki, "Design of a compliant press-fit connection", IEEE Transactions on components, hybrids, and manufacturing technology, vol. CHMF-A, 1985.
- [Kob89] S. Kobayashi, S.-I. Oh, T. Altan, Metal forming and the Finite-Element Method. Oxford series on advanced manufacturing, Oxford University Press, New York, 1989.

- [Kra65] I. V. Kragelskii, *Friction and Wear*. London Butterworths, 1965.
- [Len55] R. E. Lenhard, "The relationship of hardness measurements to the tensile and compression flow curves", WADC Technical Report, vol. 114, 1955.
- [Mac03] J. Mackerle, "Finite element analysis of fastening and joining: A bibliography (1990-2002)", *International journal of pressure vessels and piping*, vol. 80, pp. 253-271, 2003.
- [Man07] T. Manninen, K. Kanervo, A. revuelta, J. Larkiola, A.S. Korhonen, "Plastic deformation of solderless press-fit connectors", *Materials Science and engineering A* 460-461, pp. 633-637, 2007.
- [Mar6] T. Marquardt. *Numerische Simulation des Small-Punch-Tests*, MPA Stuttgart, 2006.
- [Mer01] H. Mercado-Corujo, "A study od thermo-mechanical reliability of plated-through-hole/ press-pin assemblies", M.Sc. Thesis, Georgia Institute of Technology, Mechanical Engineering, 2001.
- [Mit04] B. S. Mitchell, *Materials engineering and science for chemical and materials engineers*. John Wiley & Sons Inc., 2004.
- [Mor04] A. Morawiec, *Orientations and rotations: computations in crystallographic textures*. Springer, 2004.
- [Naa87] H. Naaman, R. Talreja, D. Juul Jensen, N. Hansen, "Development of deformation textures in polycrystalline copper. Experiments and model

- predictions”, Textures and Microstructures, vol. 7, pp. 149-170, 1987.
- [Nag67] N. Nagata, S. Yoshida, “Deformation of copper single crystals and polycrystals at high strain rates”, J. Japan Inst. Metals, vol. 31, 1967.
- [NAS10] L. Nasdala, FEM-Formelsammlung Statik und Dynamik. Vieweg + Teubner, Wiesbaden, 2010.
- [Neu03] T. Neumeier, “Zur Optimierung der Verfahrenswahl von Kalt-, Halbwarm- und Warmmassivumformverfahren”, Fortschritt-Berichte VDI, 2003.
- [Ngu00] V. S. Nguyen, K. P. Herrmann, W. H. Müller, H. J. Albrecht, J. Foulds, “Determination of mechanical parameters of solder materials using the miniature measuring method Small Punch Test”, Mikromat Conference, pp. 671-674, Berlin, 2000.
- [Nob04] J. P. Nobre, A. M. Dias, M. Kornmeier, “An empirical methodology to estimate a local yield stress in work-hardened surface layers”, Society for Experimental Mechanics, vol. 44, 2004.
- [Nol74] H. Nolle, R. S. H. Richardson, “Static friction coefficient for mechanical and structural joints”, Wear, vol.28, pp. 1-13, 1974.
- [Nol94] R. Nolde, Einpresstechnik: Eine praxisnahe Einführung. Eugen G. Leuze Verlag, 1994.
- [Par03] H. Parisch, Festkörper-Kontinuumsmechanik. B.G. Teubner Verlag, 2003.
- [Per00] B. N. J. Persson, Sliding Friction: Physical Principles and Applications. 2nd edition, Springer, 2000.

- [Pet03] J. Petruska, L. Janicek, “On the evaluation of strain inhomogeneity by hardness measurement of formed parts”, *Journal of Materials Processing Technology*, vol. 143, pp. 300-305, 2003.
- [Pop11] V. L. Popov, *Kontaktmechanik und Reibung*. 2th edition, Springer Verlag, 2011.
- [Rös12] J. Rösler, H. Harders, M. Bäker, *Mechanisches Verhalten der Werkstoffe*. 4th edition, Springer Vieweg, 2012.
- [Sch98] H. Schafstall, *Verbesserung der Simulationsgenauigkeit ausgewählter Massivumformverfahren durch eine adaptive Reibwertvorgabe*, PhD Thesis Universität der Bundeswehr Hamburg, 1998.
- [Smi04] *Smithells Metals Reference Book*. Ed. by W. F. Gale and T. C. Totemeier, 8th edition, Elsevier, 2004.
- [Son07] F. O. Sonmez, A. Demir, “Analytical relations between hardness and strain for cold formed parts”, *Journal of Materials Processing Technology*, vol. 186, 2007.
- [Sta11] D. Stamenkovic, M. Milosevic, M. Mijajlovic, M. Banic, “Estimation of the static friction coefficient for press fit joints”, *Journal- Balcan Tribological Association*, vol. 17, pp. 341-355, 2011.
- [Sta11] D. Stamenkovic, M. Milosevic, M. Mijajlovic, M. Banic, “Estimation of the static friction coefficient for press fit joints”, *Journal- Balcan Tribological Association*, vol. 17, pp. 341-355, 2011.
- [Ste08] U. Stelzmann, C. Groth, *FEM für Praktiker-Strukturmechanik: Basiswissen und Arbeitsbeispiele zu*

- FEM-Anwendungen der Strukturdynamik. Expert Verlag, 2008.
- [Sun94] G. Sundarajan, Y. Tirupataiah, “The hardness- flow stress correlation in metallic materials”, Bulletin of Materials Science, vol. 17, pp. 747-770, 1994.
- [Tab51] D. Tabor, “The hardness and strength of metals”, Journal of the Institute of Metals, vol. 79, pp. 1-18, 1951.
- [Tek00] A. E. Tekkaya, K. Lange, “An improved relationship between Vickers hardness and yield stress for cold formed materials and its experimental verification”, CIRP Annals- Manufacturing Technology, vol. 49, pp. 205-208, 2000.
- [Toh06] H. Tohnyoh, K. Yamanobe, M. Saka, J. Utsumomiya, T. Nakamura, Y. Nakano, “Determination of friction coefficient of a press-fit pin in thin plating”, JSME International Journal, vol. 49, 2006.
- [VDI04] “Methodische Auswahl fester Verbindungen-Systematik, Konstruktionskataloge, Arbeitshilfen”, Ref. Nr. VDI 2232:2004-01, VDI-Gesellschaft Entwicklung Konstruktion Vertrieb, 2004.
- [Vin88] O. Vingsbo, M. Sonderberg, “On fretting maps”, Wear, vol. 126, pp. 131-174, 1988.
- [Wag99] G. Wagner, Plastische Verformung von LiF-Einkristallen, polykristallinem Kupfer und Stahl. University of Augsburg, 1999.
- [Wat72] R. B. Waterhouse, Fretting Corrosion. Pergamon, Oxford, 1972.

- [Wie98] Wieland-Kupferwerkstoffe: Herstellung, Eigenschaften und Verarbeitung. Süddeutsche Verlagsgesellschaft Ulm, 1998.
- [Wit08] K. Wittig, “Erfahrungen mit der Einpresstechnik für die elektronische Baugruppen in der Automotive-Anwendung”, Systemintegration in der Mikroelektronik, 2008.
- [Wri11] S. I. Wright, M. M. Nowell, D. P. Field, “A Review of Strain Analysis using EBSD,” *Microscopy and Microanalysis*, vol. 17, pp. 316-329, 2011.
- [Xie00] W. Xie, E. C. De Meter, M. V. Trethewey, “An experimental evaluation of coefficients of static friction of common workpiece-fixture element pairs”, *International Journal of Machine Tools and Manufacture*, vol. 40, pp. 467-488, 2000.
- [Yam90] S.E. Yamada, H. Ueno, “Analysis of insertion force in elastic/plastic mating”, *Journal of electronic packaging*, vol. 112/3, 1990.
- [Yap07] G. G. Yapici, I. J. Beyerlein, I. Karaman, C. N. Tomé, “Tension-compression asymmetry in severely deformed pure copper”, *Acta Materialia*, vol. 55, pp. 4603-4613, 2007.

Appendix A

Sample preparation and analysis

Light microscope pictures

The microstructure of the samples was made visible for the light microscope pictures as defined in Table A.1.

Table A.1: Preparation for light microscope pictures. Samples were embedded in a cold epoxy material.

Grinding	Silicon carbide abrasive paper up to 2500 granulation
Polishing	6 min, 9 μm diamant suspension
	3 min, 3 μm diamant suspension
	3 min, 1 μm diamant suspension
Etching	Iron (III) chloride based chemical etching

An Olympus BX43 fluorescence microscope was the equipment used for the analyses.

EBSD experiments

The procedure presented in Table A.2 was applied for the stress-free preparation of the surfaces for EBSD experiments.

Table A.2: Preparation for EBSD experiments. Samples were embedded in a cold epoxy material for their preparation and released from it before the measurements for a better electrical contact.

Grinding	Silicon carbide abrasive paper up to 2500 granulation
Electro-polishing	Phosphoric acid based electrolyte. 24 V, during 20''

Electron-Backscatter-Diffraction (EBSD) measurements were carried out, in order to assess texture, grain size, and work-hardening.

A dual beam Focused Ion Beam (FIB) was used (Zeiss Auriga 60, detector DigiView).

Between 34 000 and 35 000 measurements compose each EBSD scan, and a 1.5 μm step size was chosen. A grain dilation and CI standardization were applied as cleanup procedures, being 0.031 the worst case of data fraction modified after the cleanup.

Harmonic Series Expansion was used as texture calculation method. Regarding the local average misorientation angle, a kernel-based analysis method was applied, third order nearest neighbors were used, and 5° were considered the maximum misorientation.

Hardness measurements

The procedure presented in Table A.3 was applied, to reduce the preparation induced deformations in the surfaces where nanoindentation experiments were carried out.

Table A.3: Preparation for hardness measurements. Samples were embedded in a cold epoxy material.

Grinding	Silicon carbide abrasive paper up to 2500 granulation
Polishing	6 min, 9 μm diamant suspension 3 min, 3 μm diamant suspension 3 min, 1 μm diamant suspension
Vibration polishing	4 hours with a 0.05 μm colloidal suspension

The experiments were conducted in a Fischerscope HM2000 instrumented indentation equipment.

A Vickers indenter was chosen for a higher resolution of the hardness screenings. Guidelines set in DIN EN ISO 6507 and DIN EN ISO 14577 were followed for the election of indentation parameters.

Relubrication of samples

Samples were passivated with a thiol moistening (1 wt% 1-octadecanethiol) during two seconds and joined after two hours of evaporation time.